The Dynamical Impact of Electronic Thermal Conductivity on Deep Mantle Convection of Exosolar Planets

A.P. Vanden Berg, D.A. Yuen, G. Beebe, M.D. Christiansen

▶ **To cite this version:**

A.P. Vanden Berg, D.A. Yuen, G. Beebe, M.D. Christiansen. The Dynamical Impact of Electronic Thermal Conductivity on Deep Mantle Convection of Exosolar Planets. Physics of the Earth and Planetary Interiors, 2010, 178 (3-4), pp.136. 10.1016/j.pepi.2009.11.001 . hal-00610664

HAL Id: hal-00610664
https://hal.science/hal-00610664

Submitted on 23 Jul 2011

HAL is a multi-disciplinary open access archive for the deposit and dissemination of scientific research documents, whether they are published or not. The documents may come from teaching and research institutions in France or abroad, or from public or private research centers.

L'archive ouverte pluridisciplinaire **HAL**, est destinée au dépôt et à la diffusion de documents scientifiques de niveau recherche, publiés ou non, émanant des établissements d'enseignement et de recherche français ou étrangers, des laboratoires publics ou privés.

Accepted Manuscript

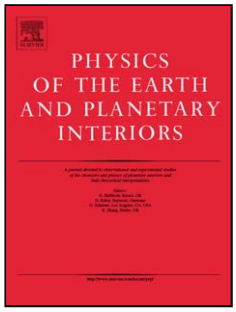

Title: The Dynamical Impact of Electronic Thermal Conductivity on Deep Mantle Convection of Exosolar Planets

Authors: A.P. vanden Berg, D.A. Yuen, G. Beebe, M.D. Christiansen

PII: S0031-9201(09)00234-9
DOI: doi:10.1016/j.pepi.2009.11.001
Reference: PEPI 5223

To appear in: *Physics of the Earth and Planetary Interiors*

Received date: 29-10-2007
Revised date: 9-11-2009
Accepted date: 11-11-2009

Please cite this article as: Berg, A.P., Yuen, D.A., Beebe, G., Christiansen, M.D., The Dynamical Impact of Electronic Thermal Conductivity on Deep Mantle Convection of Exosolar Planets, *Physics of the Earth and Planetary Interiors* (2008), doi:10.1016/j.pepi.2009.11.001

This is a PDF file of an unedited manuscript that has been accepted for publication. As a service to our customers we are providing this early version of the manuscript. The manuscript will undergo copyediting, typesetting, and review of the resulting proof before it is published in its final form. Please note that during the production process errors may be discovered which could affect the content, and all legal disclaimers that apply to the journal pertain.

*Manuscript
ACCEPTED MANUSCRIPT

The Dynamical Impact of Electronic Thermal Conductivity on Deep Mantle Convection of Exosolar Planets

A.P. van den Berg [1], D.A. Yuen [2,3]
G. Beebe [3], M.D. Christiansen[3]

[1] Dept. of Theoretical Geophysics,
Institute of Earth Sciences, Utrecht University,
3508 TA Utrecht, Netherlands.
(e-mail: berg@geo.uu.nl)
[2] Dept. of Geology and Geophysics and [3] University of Minnesota Supercomputing Institute,
University of Minnesota,
Minneapolis, MN 55455-0219, USA.
(e-mail: daveyuen@gmail.com)

submitted to Physics of the Earth and Planet Inter.

November 9, 2009

[1]

[1] Revision_0911/Revisedmanuscript

Accepted Manuscript

ACCEPTED MANUSCRIPT

Abstract

We have modelled the time-dependent dynamics of exosolar planets within the framework of a two-dimensional Cartesian model and the extended-Boussinesq approximation. The mass of the super-Earth models considered is 8 times the Earth's mass and the thickness of the mantle is 4700 km, based on a constant density approximation and a similar core mass fraction as in the Earth. The effects of depth-dependent properties have been considered for the thermal expansion coefficient, the viscosity and thermal conductivity. The viscosity and thermal conductivity are also temperature-dependent. The thermal conductivity has contributions from phonons, photons and electrons. The last dependence comes from the band-gap nature of the material under high pressure and increases exponentially with temperature and kicks in at temperatures above 5000 K. The thermal expansivity decreases by a factor of 20 across the mantle because of the high pressures, greater than 1 TPa in the deep mantle. We have varied the temperatures at the core-mantle boundary between 6000 and 10,000 K. Accordingly the Rayleigh number based on the surface values varies between 3.5×10^7 and 7×10^7 in the different models investigated. Three phase transitions have been considered: the spinel to perovskite, the post-perovskite transition and the post-perovskite decomposition in the deep lower mantle. We have considered an Arrhenius type of temperature dependence in the viscosity and have extended the viscosity contrast due to temperature to over one million. The parameter values put us well over into the stagnant lid regime. Our numerical results show that because of the multiple phase transitions and strongly depth-dependent properties, particularly the thermal expansitivity, initially most of the planetary interior is strongly super-adiabatic in spite of a high surface Rayleigh number, because of the presence of partially layered and penetrative convective flows throughout the mantle, very much unlike convection in the Earth's mantle. But with the passage of time, after several billion years, the temperature profiles become adiabatic. The notable influence of electronic thermal conductivity is to heat up the bottom boundary layer quasi-periodically, giving rise to strong coherent upwellingss, which can punch their way to the upper mantle and break up the layered convective pattern.

1 Introduction

Up to now, well over 350 exosolar planets have been discovered and their habitability has been emphasized (Haghighipohr and Raymond, 2007). According to the Extrasolar Planets Encyclopaedia (http//www.exoplanet.eu) and this list keeps on growing relentlessly. Most of these planetary bodies have been unveiled by Doppler analysis from the scattered light of the central star which reveals the wobbling of the star due to the gravitational pull of planets in close orbits (Perryman, 2000, Marcy et al., 2005, Montgomery et al, 2008, Bean et al, 2008). Most of these planets found up to now are much larger than the Earth, typically, the size of Jupiter. But recently several 'superearth' planets estimated at 5 to 10 Earth masses, dubbed Superearths, have been uncovered, near the star Gliese 876, which have been estimated about 7 Earth masses. A nearby star Gliese 581, hosts several planets. One of these labeled planet-c has a mass estimated to be around five Earth masses (http://www.solstation.com/stars/gl581.htm). Recently both size and mass were obtained of a super-Earth planet of five Earth masses, in the CoRot-7 star system, resulting in the first density estimated of a terrestrial exoplanet, similar to Earth's mean density (Queloz et al., 2009).

These astronomical discoveries have elicited tremendous interest from the geophysical and also astrophysical communities (e.g. Kokubo and Ida, 2008; Bean et al., 2008) because planets of about 5 Earth masses are not much different from Earth in size, less than a factor two, whereas they have much higher internal pressure and interior temperature. Material behavior of solid state mantle silicates under extreme P, T condition differs from the behavior experienced under Earth like deep

ACCEPTED MANUSCRIPT

mantle conditions $P < 136$ GPa, $T < 4000$ K. In particular the perovskite phase $MgSiO_3$ may dissociate in the deep mantle of superearth planets (Umemoto et al., 2005). The endothermic phase transition corresponding to this mineral dissociation appears to have a strongly negative Clapeyron slope which could induce convective layering (e.g. Honda et al., 1993) leading to reduced cooling rate for the deep mantle and core. A somewhat similar configuration with an endothermic phase transition from spinel to perovskite could occur close to the core-mantle boundary of Mars at pressure values of about 24 GPa (Breuer et al., 1997).

Due to the increased surface gravity ($g \sim 30\text{ms}^{-2}$) for a representative model planet of eigth times Earth's mass and outer radius ($R \sim 1.6R_{\oplus}$), and corresponding pressure gradient, the effective lithopheric strength of these super-earth planets is probably significantly higher than for Earth-like conditions. O'Neill and Lenardic (2007) have investigated this poignant effect on mantle dynamics where they found a clear trend towards stagnant lid convection for increasing planetary radius. This impacts the mantle convective regime and thermal history of the planet resulting in producing a higher internal temperatures and slower cooling of the interior.

Our simple density model is constrained by the given mass of the planet and we consider compressed mantle density up to 8267 kg/m^3. Valencia et al. (2007a) investigated the internal structure of Super Earth planets using values for the internal temperature derived from parameterized convection models, leading to mantle temperatures that are not much higher than for the Earth's mantle.

Here we take a different tack and use the unknown temperature contrast across the mantle ΔT as a control parameter (e.g. van den Berg and Yuen, 1998) and we investigate a range of ΔT values from 6000 K to 10000 K. A tendency towards higher mantle temperature can be expected when the planet is in the stagnant lid regime as predicted by O'Neill and Lenardic (2007). At the same time the volumetric density of radiogenic heating scales with the compressed mantle density resulting in amplification of the internal heating for a given mass concentration of radioactive isotopes. In this way our model includes the (P, T) range where Umemoto et al. (2006) predict a new phase transition where the $MgSiO_3$ postperovskite phase dissociates into the oxides. This new phase transition is predicted to be endothermic with a strongly negative Clapeyron slope of -18 MPa/K and a strong impact on mantle circulation can be expected from this phase transition.

Very high pressure, as exists in a deep super-earth mantle, also strongly reduces thermal expansivity in the planetary mantle. This increases the phase buoyancy parameter of deep mantle phase boundaries and re-enforces the degree of convective layering induced by an endothermic phase boundary (Christensen and Yuen, 1985). Estimates based on a phonon thermodynamic model for the MgO-SiO_2 system, including the $MgSiO_3$ postperovskite phase, (Jacobs, M. and B. de Jong, 2007) predict a decrease in α across the mantle with of factor of twenty (M. Jacobs, 2007, personal communication). The role of pressure dependent α has been investigated for the Earth's mantle (Hansen et al. 1994, Matyska and Yuen, 2007) and precise values of the decrease of α across the mantle is still being investigated (Katsura et al., 2009). The stronger α contrast across a super-earth mantle, considered here results in a larger tendency towards layering of deep mantle convection especially in the presence of the dissociation of post-perovskite.

Since the seminal experimental work on thermal conductivity by Hofmeister (1999) the role played by thermal conductivity in mantle convection has received a rejuvenating interest (Dubuffet et al., 1999, van den Berg et al., 2001, Dubuffett et al., 2002). But the thermal conductivity considered in those works has been concerned with modest temperature conditions. Thermal conductivity at high temperature conditions behave differently (Umemoto et al., 2006). Above about 5000 K it is strongly impacted by an electronic contribution, which behaves exponentially in temperature and

ACCEPTED MANUSCRIPT

becomes dominant in a composite conductivity model for these high temperatures (Umemoto et al., 2006).

Therefore the deep mantle dynamics of planetary evolution under high temperature and very large pressure conditions, such as may be valid for super earth planets involves complex material behavior and may be rather different from an Earth-like case, where shallow tectonics may play a more prominent role. This makes the investigation of deep mantle dynamics in exosolar planets a very interesting subject for modelling studies within a comparative planetological framework.

2 Model description

2.1 Density model

As a first approximation, we will not consider density stratification due to self-compression, though we certainly recognize their importance in modifying flow structures in the deep mantle (e.g. Jarvis and McKenzie, 1980, Zhang and Yuen, 1996). Instead we apply a simple density model of a two-layer planet with uniform density of the mantle and core ρ_m and ρ_c respectively. A uniform mantle density is consistent with the use of an extended Boussinesq approximation (e.g. Christensen and Yuen, 1985) in our convection equations as explained in section 2.2. In Appendix A expressions are given for the mantle and core radius in terms the planetary mass, known from astronomic data, and the unknown core-mantle mass ratio X_c. These expressions have been used to tabulate the planetary outer radius $R(\rho_c, \rho_m)$ for a relevant range of ρ_c, ρ_m values. This was carried out for models constrained by the planetary mass $M = 8M_\oplus$ as in the recently discovered super-earth exosolar planet orbiting the star Gliese 876.

To constrain the model further, we make some necessary assumptions concerning the overall composition and state of core mantle differentiation. We assume the overall composition to be similar as for the Earth. We further assume that early core/mantle differentiation resulted in the same core-mass fraction as for Earth $X_c = 0.315$. A contour diagram of planet outer radius $R(\rho_c, \rho_m)$ is shown in Fig. 1, for an Earth-like value of $X_c = 0.315$.

Several special model cases are shown in Fig.1, labeled $m1, \ldots, m5$, indicated by separate symbols. Dimensional parameter values for these models are listed in Table 1.

Model $m1$ represents a uniform density case, $\rho_c = \rho_m = \rho_\oplus$, without core mantle differentiation, where the uniform density is equal to Earth's mean density, with an outer radius of twice the Earth radius.

The other models $m2, \ldots, m5$ are located on the dashed line of constant $\rho_c/\rho_m = 2.35$. This ratio corresponds to the value for a two-layer model with homogeneous mantle and core, constrained by the Earth's total mass and moment of inertia factor. Model $m2$ is defined by setting the constraint $R' = 2$ and $\rho_c/\rho_m = 2.35$. Substitution of the known parameters in the expression (15) for R'_c gives $R'_c = 1.094$. Substitution of the value for R'_c in the expression for ρ'_c (16) gives $\rho'_c = 1.9246$. Finally substituting in the expression for the mantle density (17) gives $\rho'_m = 0.81905$. Models $m3, \ldots, m5$ are obtained by applying an increasing uniform compression factor $f > 1$ to the core and mantle densities, keeping a constant ratio $\rho_c/\rho_m = 2.35$. f is defined to be the ratio of the core or mantle density of the different model cases listed in Table 1, $m_j, j = 1, \ldots, 5$, with respect to the corresponding core or mantle density of model $m3$.

Accepted Manuscript

ACCEPTED MANUSCRIPT

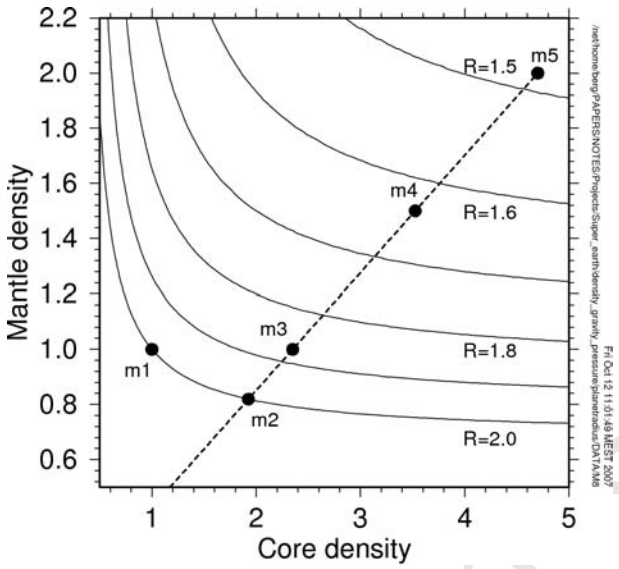

Figure 1: *Planetary radius as a function of non-dimensional core and mantle density (scale value* $\rho_\oplus = 5511\text{kgm}^{-3}$*) for models constrained by* $M = 8M_\oplus$ *and* $X_c = X_{c\oplus} = 0.315$*. The dashed line represents the subset of models with increasing uniform compression factor* f *(see column 2 in Table 1) with a fixed density ratio* $\rho_c/\rho_m = 2.35$*. The labeled symbols* $m1, \ldots, m5$ *refer to the model cases listed in Table 1.*

model #	f –	R /1000 km	R_c /1000 km	ρ_m kg/m^3	ρ_c kg/m^3	$g(R)$ m/s^2	$g(R_c)$ m/s^2	$P(R_c)$ GPa	$P(0)$ GPa
$m1$	-	12.742	8.6698	5511.4	5511.4	19.63	13.36	370.168	689.2739
$m2$	0.819	12.742	6.9699	4514.1	10607.	19.36	20.67	493.226	1257.117
$m3$	1.0	11.922	6.5212	5511.4	12951.	22.42	23.60	643.673	1640.580
$m4$	1.5	10.415	5.6968	8267.1	19426.	29.38	30.93	1105.25	2816.934
$m5$	2.0	9.4623	5.1759	11023.	25901.	35.60	37.47	1621.88	4133.753

Table 1: *Dimensional parameters of models* $m1 \ldots m5$*, corresponding to the discrete symbols in Fig. 1. The table includes the surface- and core-mantle boundary values of the gravity accelleration* $g(R)$ *and* $g(R_c)$ *and the values of the static pressure at the CMB and in the centre of the planet* $P(R_c)$ *and* $P(0)$*.*

The scaling of the surface gravity with the planet radius R for the models located on the dashed line in Fig. 1 is shown in Fig. 2(a). The surface gravity increases non-linearly with the planetary radius as shown the left hand frame. Model case $m4$ with surface gravity 29.38 m/s^2 and a CMB pressure of 1.105 TPa has been used in the mantle convection experiments. At this CMB pressure the dissociation of post-perovskite can be expected to have taken place for sufficiently high temperature (Umemoto et al., 2006). Fig. 2(b) shows the radial distribution of the gravity accelleration $g(r)$ in the mantle and top of the core, for model case $m4$. The peak to peak variation of g is less than 10% in the mantle and we have used a uniform value of g equal to the surface value in our convection calculations. A relatively uniform mantle gravity value reflects the connection between our model and the Earth's mantle resulting from the given model assumptions, in particular for an Earth-like core mass fraction. Planets with a much smaller core mass fraction show a significantly

ACCEPTED MANUSCRIPT

greater variation of $g(r)$, with zero valued central gravity for a planet without a core. In general, low gravity values will impact the style of convection and may lead to increased layering in a similar way as a strong decrease of thermal expansivity with pressure from considerations of experimental equation of state (Katsura et al, 2009).

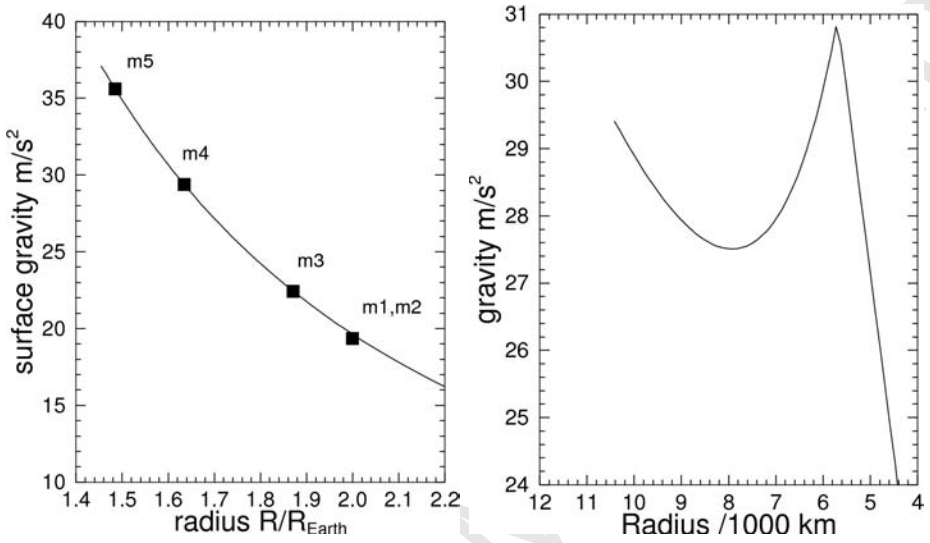

Figure 2: *(a)(Left) surface gravity as a function of planet size (outer radius R) for the models constrained by* $M = 8M_{\oplus}$, $X_c = X_{c\oplus} = 0.315$ *and varying uniform compression with a fixed density ratio* $\rho_c/\rho_m = 2.35$. *Discrete symbols correspond to the models* $m1, \ldots, m5$ *shown in Fig.1 and Table 1. (b)(Right) radial distribution of gravity accelleration for model* $m4$.

2.2 Convection model

The governing equations of the numerical model express conservation of mass momentum and energy in the extended Boussinesq formulation. We have also used a 2-D Cartesian model for a planetary body, which is another gross simplification. Symbols used are explained in Table 2.

$$\partial_j u_j = 0 \tag{1}$$

$$-\partial_i \Delta P + \partial_j \tau_{ij} = Ra \left(\alpha T - \sum_j \frac{Rb_j}{Ra} \Gamma_j \right) \delta_{i3} \tag{2}$$

$$\tau_{ij} = \eta(T,P) \left(\partial_j u_i + \partial_i u_j \right) \tag{3}$$

$$\frac{DT}{Dt} = \partial_j \left(\kappa(T,P) \partial_j T \right) + \alpha Diw(T + T_0) + \sum_j \gamma_j \frac{Rb_j}{Ra} Di \frac{D\Gamma_j}{Dt}(T + T_0) + \frac{Di}{Ra}\Phi + R_H H(t) \tag{4}$$

The continuity equation (1) describes mass conservation of the incompressible fluid model. Conservation of momentum is expressed in the Stokes equation (2) based on the infinite Prandtl number assumption. The rheological constitutiive equation (3) defines the temperature and pressure dependent linear viscous rheology. Two types of viscosity models are applied in different model cases, an

ACCEPTED MANUSCRIPT

exponential parameterization in terms of layer viscosity contrasts and the temperature, commonly called the Frank-Kamentzky approximation and an Arrhenius type parameterization in terms of activation parameters of the form exp(E*/RT), where E* is the activation free energy, R is the gas constant and T is the absolute temperature. Details of the parameterizations used are given in in Table 2. Energy transport is governed by (4), where the righthand side terms are for thermal diffusion, adiabatic heating, latent heat of phase transitions, viscous dissipation and radiogenic internal heating respectively.

Multiple phase transitions are implemented using an extended Boussinesq formulation through phase parameter functions $\Gamma_j(P,T)$, which parameterize the Clapeyron curves in the phase diagram. This is expressed in the equation of state (Christensen and Yuen, 1985),

$$\rho = \rho_0 \left(1 - \alpha(T - T_{surf}) + \sum_j \Gamma_j \frac{\delta\rho_j}{\rho_0}\right) \tag{5}$$

We apply a composite temperature and pressure dependent conductivity model which contains contributions from phonon (k_{lat}), photon (k_{rad}), (Hofmeister, 1999) and electron k_{el} transport (Umemoto et al., 2006).

$$k(T,P) = k_{lat}(T,P) + k_{rad}(T) + k_{el}(T) \tag{6}$$

The contributions of k_{lat} and k_{rad} are modified versions of an earlier work (van den Berg et al., 2005), which was based on the Hofmeister (1999) model.

$$k^*_{lat} = k_0 \left(\frac{T_{surf}}{T}\right)^a \times \exp\left[-\left(4\gamma + \frac{1}{3}\right)\alpha(P)(T - T_{surf})\right] \times \left(1 + \frac{K_0' P}{K_0}\right) \tag{7}$$

Symbols used in the parameterization of the conductivity are explained in Table 3. The parameterization of the pressure dependence of the phonon conductivity in (7) would make it the dominant contribution for Earth-like deep mantle conditions. In the present model applied to super-earth conditions we assume saturation of the phonon contribution above a temperature of about 4000 K where we apply a smooth truncation to an upper limit value of $k_{trunc} = 15$ $\mathrm{Wm^{-1}K^{-1}}$. To this end the original lattice component k^*_{lat} has been modified by introduction of a smooth truncation at a preset upper limit k_{trunc},

$$k_{lat} = \left((k^*_{lat})^{-2} + (k_{trunc})^{-2}\right)^{-1/2} \tag{8}$$

The original polynomial representation of k_{rad} of Hofmeister (1999) shows serious anomalies for temperatures above about 5000 K. Therefore we replaced this polynomial parameterization by a simple parameterization, where $k_{rad}(T)$ is set to a uniform value of $k_{rad} = 2$ $\mathrm{Wm^{-1}K^{-1}}$ in an operational temperature window and tapered off to zero on both sides of this window using harmonic (sine function) tapers with corner temperatures specified in Table 3.

The conductivity component from electron transport is parameterized as,

$$k_{el} = k_{ep} \exp\left(-\frac{E_{el}}{k_B T}\right) \tag{9}$$

where k_B is Boltzmanns constant and the activation energy is set to $E_{el} = 3$ eV. The prefactor value for k_{ep}, defined in Table 3, is obtained from an estimated reference conductivity at 10000 K of 40 $\mathrm{Wm^{-1}K^{-1}}$ (Umemoto et al.,2006).

Accepted Manuscript

ACCEPTED MANUSCRIPT

The different components of the composite conductivity model are shown for relevant temperature and pressure values in Fig. 3. Frames (a) and (b) show the distributions of the electron conductivity and radiative conductivity respectively which are independent of pressure. The electron conductivity becomes operational above a temperature of 5000 K. In the parameterization of k_{rad} the upper cut-off temperature has been set at 5000 K. Frame (c) shows isobaric temperature distributions at four different pressure values, of the lattice conductivity component. The lattice conductivity has been truncated at high pressure at a value of 15 $\mathrm{Wm^{-1}K^{-1}}$. The corresponding total effective conductivity values are shown in frame (d).

The coupled equations (1), (2), (4), are solved on a 2-D rectangular domain of aspect ratio 2.5. Finite element methods are used (van den Berg et al., 1993) based on the SEPRAN finite element package (Segal and Praagman, 1994) to solve the equations. The boundary conditions used are: free slip, impermeable conditions on all boundaries. The temperature at the horizontal boundaries are constant with a fixed temperature contrast ΔT across the layer driving thermal convection. Zero heat-flux conditions apply to the vertical boundaries. By prescribing a constant temperature at the CMB in our model we have not included thermal coupling between the mantle and the core heat reservoir.

The initial condition for the temperature for all model runs was obtained from a non-dimensional temperature snapshot of a time dependent convection run with representative parameters. Profiles of the initial temperature are shown in the results section in Fig. 12.

The finite element mesh consists of 45,451 nodal points, 151 points vertical and 301 points in the horizontal direction. The nodal points span 22,500 quadratic triangular elements for the Stokes equation. Each Stokes element is subdivided in four linear triangles for the energy equation.

The time-dependent energy equation drives the time integration which is based on a predictor corrector method employing an implicit Euler predictor and a Crank-Nicolson corrector step in a second order correct integration scheme. An adaptive time step has been used equal to half the Courant time step.

Accepted Manuscript

ACCEPTED MANUSCRIPT

Symbol	Definition	Value	Unit
h	Depth of the mantle model	$4.7 \cdot 10^6$	m
z	Depth coordinate aligned with gravity	-	-
P	Thermodynamic pressure	-	-
$\Delta P = P - \rho_0 g z$	Dynamic pressure	-	-
T	Temperature	-	-
T_{surf}	Surface temperature	573	K
ΔT	Temperature scale	$6000 \leq \Delta T \leq 10000$	K
u_i	Velocity field component	-	-
$e_{ij} = \partial_j u_i + \partial_i u_j$	strain rate tensor	-	-
$e = [1/2 e_{ij} e_{ij}]^{1/2}$	Second invariant of strain rate	-	-
w	Vertical velocity aligned with gravity	-	-
$\eta_{exp}(T,z) = \eta_0 \exp(cz - bT)$	Exponential viscosity model	-	Pa s
	$b = \ln(\Delta\eta_T), c = \ln(\Delta\eta_P)$		
	where $\Delta\eta_T = 300, \Delta\eta_P = 100$ are		
	viscosity contrasts due to T and P	-	
η_0	Viscosity scale value	$2.5 \cdot 10^{23}$	Pa s
$\eta_{Arr}(P,T) = B \exp\left(\frac{E+PV}{RT}\right)$	Arrhenius viscosity model	-	Pa s
B	Viscosity prefactor	$4.98 \cdot 10^{17}$	Pa s
E	Activation energy	$3 \cdot 10^5$	J/mol
V	Activation volume	$0.5 \cdot 10^{-6}$	m^3/mol
R	Gass constant	8.3144	$JK^{-1}mol^{-1}$
$\tau_{ij} = \eta e_{ij}$	Viscous stress tensor	-	-
$\Phi = \eta e^2$	Viscous dissipation function		-
$\alpha(z) = \frac{\Delta\alpha}{[c(1-z)+1]^3}$	Depth dependent thermal expansivity		-
$\Delta\alpha = \alpha(1)$	Expansivity contrast across the layer	0.1-0.05	-
$c = \Delta\alpha^{1/3} - 1$		-	-
α_0	Thermal expansivity scale value	$4 \cdot 10^{-5}$	K^{-1}
ρ	Density	-	-
ρ_0	Density scale value	8.267	kgm^{-3}
c_p	Specific heat	1250	$JK^{-1}kg^{-1}$
k	Thermal conductivity	-	-
k_0	Conductivity scale value	4.7	$Wm^{-1}K^{-1}$
$\kappa = \frac{k}{\rho c_p}$	Thermal diffusivity	-	-
g	Gravitational acceleration	30	ms^{-2}
$Ra = \frac{\rho_0 \alpha_0 g \Delta T h^3}{\kappa_0 \eta_0}$	Thermal Rayleigh number	-	-
$Rb_j = \frac{\delta\rho_j g h^3}{\kappa_0 \eta_0}$	Rayleigh number j^{th} phase transition	-	-
$\delta\rho_j$	Density increment j^{th} phase transition	-	kgm^{-3}
$\Gamma_j = \frac{1}{2}\left(1 + \sin\left(\frac{\pi(z - z_{0j})}{\delta z}\right)\right)$	Phase parameter j^{th} phase transition	-	-
$z_{0j} = \left(P_{ref}^{(j)} + \gamma_j \left(T - T_{ref}^{(j)}\right)\right)/(\rho_0 g)$	Depth j^{th} phase transition	-	-
γ_j	Clapeyron slope j^{th} phase transition	-	-
δz	Half width of the phase transitions	100	km
$Di = \frac{\alpha_0 g h}{c_p}$	Surface dissipation number	4.53	-
$R_H = \frac{H_0 h^2}{c_p \kappa_0 \Delta T}$	internal heating number	$10 \leq R_H \leq 17$	
H_0	density internal heating	$2.55 \cdot 10^{-12}$	Wkg^{-1}

Table 2: Physical parameters

Accepted Manuscript

ACCEPTED MANUSCRIPT

Symbol	Definition	Value	Unit
k	Thermal conductivity	-	-
k_0	Conductivity scale value	4.7	$\mathrm{Wm^{-1}K^{-1}}$
a	Conductivity power-law index	0.3	-
γ	Grueneisen parameter	1.2	-
K_0	Bulk modulus	261	GPa
$K_0{}'$	pressure derivative of bulk modulus	5	-
k_{trunc}	truncation value of k_{rad}	15	$\mathrm{Wm^{-1}K^{-1}}$
$T_i, i = 1, \ldots, 4$	corner temperatures k_{rad} taper	$573, 4000, 4500, 7000$	K
E_{el}	activation energy electron transport (3 ev)	$3 \cdot 1.6 \cdot 10^{-19}$	J
k_B	Boltzmann constant	$1.38 \cdot 10^{-23}$	J/K
k_{ep}	electron conductivity prefactor	487.54	$\mathrm{Wm^{-1}K^{-1}}$

Table 3: Parameters describing the conductivity model.

3 Results from numerical experiments

Six models with contrasting parameters will be investigated which show characteristic features for the extremely high temperature and pressure regime, which prevails in the deep mantle of a putative super-earth model with a mass eight times the Earth's mass. Three phase transitions involving the silicates are included in these models the parameters of which are listed in Table 4. These are an endothermic phase transition near 24 GPa corresponding to the transition from the γ spinel polymorph of olivine to perovskite and an exothermic transition near 125 GPa from perovskite to post-perovskite (Tsuchiya et al., 2004). The third transition from post-perovskite to a new extremely high pressure phase 3PO, which consists of periclase and silicon oxide, is strongly endothermic $\gamma =$ -18 MPa/K and occurs at a reference pressure and temperature of 1000 GPa and 7000 K, i.e. near the core-mantle boundary (CMB) of the super-earth models, situated at 1.17 TPa, (Umemoto et al, 2006).

	P_{ref} GPa	T_{ref} K	γ MPa/K	$\delta\rho/\rho_0$ %
$P1$	23.6	2000	-1.8	7.5
$P2$	125	2750	7.2	1.5
$P3$	1000	7000	-18	2

Table 4: Parameters of the phase transitions.

In the presentation of the modelling experiments, we have devoted our attention on the role of the 3PO phase transition in the dynamics of mantle convection. We investigate in particular the interplay of several thermal conductivity and thermal expansivity models with the 3PO phase transition controling the convective layering.

Our emphasis is to study the influence of the variations of physical properties on the style of exo-solar planetary convection under extreme conditions.

The characteristic parameters of the models being investigated, which are labeled A,B,C,D,E and F, are given in Table 5.

Accepted Manuscript

ACCEPTED MANUSCRIPT

Model	Expansivity contrast $\Delta\alpha$	conductivity model $k(T,P)$	Clapeyron slope 3PO γ MPa/K	Viscosity type
A	0.1	k_0	-18	exponential
B	0.05	k_0	-18	exponential
C	0.05	$k_{lat}+k_{rad}+k_{el}$	-18	exponential
D	0.05	$k_{lat}+k_{rad}+k_{el}$	0	exponential
E	0.05	$k(z)$	-18	exponential
F	0.05	$k_{lat}+k_{rad}+k_{el}$	-18	Arrhenius

Table 5: Characteristic parameters of the convection models investigated.

The temperature at the CMB is kept at a constant value in these models. The unknown temperature contrast across the mantle ΔT is treated as a control parameter and we have investigated model behavior for the cases specified in Table 5 at three contrasting ΔT values, $6000, 8000, 10,000$ K respectively. Higher temperature contrasts than the estimated 4000 K for the Earth's mantle are in line with a higher volume/surface ratio of the larger planet investigated. Besides bottom heating, we have included internal heating from radioactive decay at a constant value of 2.5×10^{-12} W/kg, resulting values of the internal heating number R_H, defined in Table 2, vary between 10 and 17. We regard this range to be a speculative conjecture.

In Fig. 4 representative snapshots of the temperature field and corresponding streamfunction field are shown for model cases A,B,C defined in Table 5, with the same temperature contrast $\Delta T = 10,000$ K.

Instantaneous positions of the three phase boundaries are indicated by the white lines. The depths of the first two phase transitions are much smaller than in the Earth's mantle due to the much greater pressure gradient resulting from the high density ($\rho = 8.29$ kg/m^3) and gravity acceleration $g = 29.4$ ms^{-2} derived in section 2.1. Phase boundary topography is also directly affected by the large pressure gradient of the exosolar planet. This is the reason that the peak to peak amplitude of the topography on the 3PO phase boundary is limited to a value of 170 km in spite of the fact that the relevant Clapeyron slope has a very high magnitude of 18 MPaK^{-1}.

The different degree in the style of layered convection near the bottom 3PO phase boundary can be clearly discerned in these frames, in particular in the distribution and spacing of the contour lines in the streamfunction. Model A with a decrease factor of thermal expansivity across the mantle $\Delta\alpha = 0.1$ shows limited interaction between the endothermic 3PO phase boundary, with hot plumes crossing the phase boundary in several locations. A whole mantle flow pattern is indicated by the complete circuits of the streamfunction with highest velocities related to three cold descending flows emerging from the top boundary.

The middle row of snapshots for model B with, $\Delta\alpha = 0.05$, illustrates a penetrative convective flow regime in the streamfunction with flow concentrated in the top half of the mantle and the bottom circulation is being driven by the convection cells in the shallow mantle. As in the A model the flow is driven by the cold downwellings. The temperature snapshots reveal an increased layering at the 3PO boundary at the bottom, as indicated by the mushroom shaped plumes, which show only limited penetration of the deepest phase boundary. The increase in layering between models A and B is related to the smaller value of the thermal expansivity near the 3PO phase transition resulting in a higher effective phase buoyancy parameter that scales inversely with respect to α (Christensen and Yuen, 1985). Similar layered penetrative convection was observed in Breuer et al. (1997) in a model for the Martian mantle.

Accepted Manuscript

ACCEPTED MANUSCRIPT

In contrast to the constant thermal conductivity models A,B model C has a variable thermal conductivity $k(T, P)$ model with a strong contribution from electron thermal conductivity k_{el} near the bottom of the mantle, where temperatures are in excess of 5000 K (see Fig. 13, 14, 15). The high conductivity at the base of the mantle results in an increased heat flow into the bottom 3PO layer, producing episodic occurence of massive mantle plumes that break through the phase boundary, as illustrated by the hot plume near the middle of the temperature frame and corresponding high vertical velocity shown by the close spacings in the streamfunction.

In order to investigate the contrasting dynamics of the bottom layer of the different models we have applied passive tracer particles to monitor the relevant physical fields. To this end we have staged a set of 2000 randomly distributed tracer particles which are advected by the convective flow. The instantaneous coordinates, temperature and mineral phase in the tracer positions were stored at every integration time step. To reinforce further the impact of different parameterizations on the deep mantle dynamics, in particular on the convective layering near the bottom 3PO phase region, we present statistics and space-time trajectories of tracer particles in Fig. 5, for the B and C models. Tracer residence times for the bottom 3PO layer were calculated for the duration of the model runs of 3.2 Gyr. Histograms illustrating different statistics of the tracer residence times are shown in frames (a) and (b). Residence times attain higher values in model case B in agreement with a more layered type of convection. This agrees also with the higher values of the (clipped) first bin for case B, representing tracers that have been confined to the layers overlying the 3PO phase region.

Trajectories for four representative tracers from representative bins of $\tau \sim 1$ Gyr (C model) and $\tau \sim 3$ Gyr (B model) are shown in frames (c) and (d). For the same tracers of (c) and (d), corresponding time series of the height above the CMB are displayed in frames (e) and (f). From (c) and (f) we see that the C-model tracers with $\tau \sim 1$ Gyr have been deposited in the 3PO layer in the early history where they remain for about 1 Gyr. After this time they were advected into the overlying postperovskite layer where they mix througout the domain without returning to the 3PO region except for a short excursion of a single tracer at 2.5 Gyr. The removal of the four tracers from the 3PO layer coincides with a flushing event related to the hot plume penetrating the 3PO phase boundary shown in Fig. 4(C). In contrast to this frame (d) and (f) show trajectories from the B model results for tracers taken from the residence time bin at 3 Gyr. These tracers are moved into the bottom 3PO layer in the early history where they remain for the remainder of the model run time, in agreement with the more isolated character of the bottom layer corresponding to the greater convective layering observed for this case.

From the tracer records the coordinates and time values of the 3PO phase boundary crossings were determined for upward and downward crossings separately. An estimate of the volume flux through the phase boundary is given by the number of phase boundary crossings in a given time window normalized by the total number of tracers in the domain (van Summeren et al., 2009). Fig. 6a shows an x, t plot of the tracer phase boundary crossings for model C. This figure illustrates that the 3PO transition is a leaky boundary for mantle convective flow for this model case. Mass transport through the boundary is characterized by localized hot plumes and broader regions of return flow by cold downwellings. Episodic behavior of the plume dynamics suggested by the VRMS curve of Fig.16 later in this section is reflected in the clusters of hot upward boundary crossing events that emerge at several x-locations. The two event clusters at $t \sim 1.1$ Gyr and dimensionless x-coord ~ 1.2 and 1.8 are associated with two plumes breaking through the 3PO boundary shown in Fig.4. This dynamic episode can also be identified in a corresponding peak value of the VRMS curve shown in Fig.16.

ACCEPTED MANUSCRIPT

Temporal variation of mass transport through the 3PO boundary is quantified in frame (b). This figure shows the number of upward crossing events accumulated in 100 Myr time bins normalized by the total number of particles as an estimate of the fractional volume flux involved. The maximum flux values coiincide with the episodic clusters of hotplumes breaking through the boundary. Up to 5% of the mantle volume crosses the 3PO boundary per 100 Myr for this particular case.

Fig. 6c shows the temperature distribution of upward flowing tracers crossing the depth of 90% of the domain depth, about halfway the 3PO layer. There is a clear correlation with the (red) upward 3PO bondary crossings in frame (a). The temperature of the emerging hot upwellings at $x = 1.2$ and $x = 1.8$ increases towards the time of plume breakthrough $t \sim 1.1\ Gyr$. This is followed by a drop of the observed temperature and subsequent gradual increase in agreement with an episodic convective style.

Several physical effects interact in creating the dynamics of the 3PO layer. In particular the conductivity model and strongly endothermic phase transition, reinforced by a low value of the thermal expansivity, $\sim 5\%$ of the surface value, play a role in controling the episodic behavior. To separate these different effects we have investigated two contrasting models were the parameters were chosen to exclude a single effect. These are the constant conductivity model B and a variable conductivity model D with a zero Clapeyron slope of the 3PO transition. Fig. 7 shows results for both these models B (left) and D (right). Mass transport through the 3PO boundary is significantly smaller for the constant conductivity model B (Fig. 7 left hand) than for the variable conducivity model C (Fig. 6). This is quantified by the total number of phase boundary crossing events for the B model which is less then 50% of the C model value. This is in agreement with the snapshot of the temperature and streamfunction field shown in Fig.4B, suggesting a layered convective flow regime for the bottom 3PO region with weak leakage through the boundary near x-coordinate 0.7 at the snapshot time $1.2Gyr$.

The right hand frames of Fig. 7 show the result of removing the dynamical effect of the endothermic phase boundary by setting the Clapeyron slope to zero, while maintaining the variable thermal conductivity. The number of phase boundary crossings has strongly increased with respect to model C and the dynamics are controlled by stable cold downwellings instead of episodic hot plumes.

Comparison of the results of models B, C and D shows that the strongly endothermic phase transition is the essential ingredient for the layering of the flow in the 3PO region and that the effect of the highly variable conductivity is to produce a weakening of the convective layering and introduction of episodic behavior of the layering.

The latter effect can be understood by comparing the contrasting wavelength structure of the lateral variations of temperature in the 3PO layer between models B and C as shown in Fig.4B,C. The temperature field of the variable conductivity results is clearly dominated by longer wavelengths (Matyska et al., 1994) than the corresponding constant conductivity snapshot. An increase in the dominant wavelength of lateral variations of temperature decreases the stability of phase induced convective layering (Tackley, 1995).

The mechanism described above results from a more or less constant (in time) high effective conductivity value in the bottom layer including the phase boundary, comparable to a downward shift of the local Rayleigh number with well known impact on the phase induced convective layering (Christensen and Yuen, 1984). To test this explanation we did a model run, labeled E in Table 5, with a purely depth dependent conductivity model defined by a depth profile obtained from time averaging snapshots of horizontally averaged conducitvity profiles of model C (van den Berg et al., 2005). The results of this model run, shown in Fig. 8, confirm the equivalent dynamics of the C

ACCEPTED MANUSCRIPT

and E models, and the dominant role of the horizontal average conductivity profile. The dynamical similarity between the C and E models is further illustrated in the temperature snapshot of Fig. 9. This figure, almost identical to Fig.4C, shows two hot plumes breaking through the 3PO boundary at the model time value $1.24Gyr$ corresponding to the two red event clusters near x-coordinate values of 1.1 and 2.0.

Fig. 10 shows the representative snapshots of temperature and streamfunction for different model runs with a temperature contrast $\Delta T = 8000\ K$. The contrast between the B and C models has become smaller compared to Fig. 4 due to the smaller value of the conductivity near the bottom. This is a result of the reduced temperature and the strong temperature dependence of the electronic conductivity component which is dominant in the results shown in Fig. 4.

Model results for a smaller temperature difference of $\Delta T = 6000\ K$ are shown in Fig. 11. The same distinction holds between the A,B and C model cases as in the previous two figures with a whole mantle convection regime for the A case and penetrative convection for the models B and C. Overall the flow velocities are significantly smaller than in the previous cases for higher values of ΔT indicated by the streamfunction plots. The episodic hot plumes which occur for the C model at higher temperature contrasts are absent at the reduced $\Delta T = 6000\ K$. This is a result of the much smaller contribution of the electron conductivity for this case as illustrated in Fig. 18.

Because of their larger sizes,the exo-solar planet convection models are characterized by strongly depth-dependent properties and show clear signs of layered penetrative convection. We have therefore investigated the level of adiabaticity in the temperature distribution for two end-member values of the mantle temperature contrast ΔT of $10,000K$ and $5000K$ respectively, for the model case C of Table 5. We have compared the instantaneous temperature profiles for the two models and compared them to a reference adiabat chosen by visually matching with the time dependent geotherm. We also computed the deviation between the local temperature gradient and the adiabatic gradient

$$\beta = d < T > /dz - \alpha(z)Di(< T > +T_0) \tag{10}$$

We display the results in Figure 12. Three frames are shown for each value of ΔT, 1) for the horizontally averaged temperature profile, 2) the temperature difference with the reference adiabat and 3) the deviation from the adiabatic gradient β. The reference adiabat which was chosen by trial and error visual matching with the geotherms is added as the red-dashed line in the left-hand temperature frame. The potential temperature for the cold case is 1500K and 2750K for the hot case. The results show that the difference between the geotherm and an 'equilibrium adiabat' decays with time for both the end-member cases, thus suggesting that with sufficient mixing of the early state an adiabatic profile will be obtained but only after a time interval of two or more billion years, which is longer for lower temperature contrast across the mantle.

It looks like in the initial spin-up of the model cold material is dumped and hot material rises. Hot material is mixed rapidly in the upper half of the model as a result of the penetrative layering illustrated in the temperature and streamfunction snapshots of the previous Figures. This is illustrated by the rapid convergence of the geotherms to the reference adiabat. At the same time the bottom half is convecting much slower at least partly due to the high bottom conductivity, such that the bottom half is heating up slowly towards the adiabat. This trend is supported by the $T - T_a$ frames, showing convergence to the adiabat above a relatively substantial thermal boundary layer at the bottom with a thickness of 700 km.

Fig. 13 shows horizontally averaged profiles of temperature, viscosity and the thermal conductivity for models A,B and C. The value of the temperature contrast is $\Delta T = 10,000K$ in all cases

Accepted Manuscript

ACCEPTED MANUSCRIPT

shown. Frames (a-c) are for the variable conductivity model C. Frame (c) illustrates the strong increase of $k(T,P)$ under high T,P conditions near the bottom of the mantle. Frames (d-e) illustrate the effect of (3PO) phase induced layered convection, for the constant conductivity case B with layer contrast of thermal expansivity $\Delta\alpha = 0.05$. The layering results in a steep increase of temperature across the phase boundary (indicated by the black Clapeyron curve in the lefthand frames) and associated decrease of the slope of the viscosity profile. Frames (f-g) illustrate the model case A with constant k and $\Delta\alpha = 0.1$. There is no layering in this case with higher α and the depth profiles show little variation with respect to the initial value profiles.

In Fig. 14 similar profiles as in Fig. 13 are shown for models A,B,C for a smaller temperature contrast $\Delta T = 8000K$. The effective conductivity value for the variable k case C, shown in frame (c), is substantially smaller than in the corresponding model with $\Delta T = 10,000K$ of Fig. 13. The difference in the degree of convective layering between the three cases A,B,C is reflected in the profiles, which is similar to Fig. 13.

Fig. 15 shows corresponding profiles as in Figures 13 and 14 for model runs with $\Delta T = 6000K$. The effective thermal conductivity shown in frame (c) is now substantially smaller than in the previous Figures and the degree of convective layering is smaller than for the corresponding cases shown in Figures 13 and 14. The results here argue for the importance of electronic thermal conductivity in causing layered convection in the deep mantles of exo-solar planets.

Next we show the time-series of several global quantities for variable conductivity models of type C for different values of the temperature contrast across the mantle in Fig. 16. The basal heat-flow in Fig. 16a varies strongly between the different conductivity models, in line with the extremely strong temperature dependence of the electron conductivity. Especially for the $\Delta T = 10,000\ K$ case there is a clear correlation between the local maxima in the bottom heat flux and corresponding maxima in the rms velocity shown in the bottom frame. This is indicative of the episodic hot plumes breaking through the 3PO phase boundary as shown in the top frame of Fig. 4.

The volumetrically averaged temperature is shown in Fig. 16b. The rate of temperature increase is highest for the model with $\Delta T = 10,000$ ($\sim 200K/Gyr$) and ($\sim 30K/Gyr$) for the $\Delta T = 6000$ case. This is a consequence of the strong asymmetry in the conductivity depth profile with low surface k values and high CMB values of k resulting from the strong temperature dependence of electron thermal conductivity k_{el} (see Fig. 13, 15). Mantle heat transport is then controlled by the high thermal resistance (low k) of the top thermal boundary layer (van den Berg et al., 2005) and the high conductivity near the core mantle boundary - allowing for rapid mantle heating from the core. This is clearly illustrated in the bottom heat-flow with highest values for the model with $\Delta T = 10,000K$. This effect is amplified by the negative temperature dependence $\partial k/\partial T < 0$ of the dominant (lattice) conductivity component k_{lat} at shallow depth.

Rms velocities are shown in Fig. 16c. The Vrms curves show a change in dynamics after a initial time interval characterized by relatively low velocities below 1 cm/yr the length of which depends on the conductivity model. For the model with $\Delta T = 10,000K$ this relatively quiet period ends at about 1 Gyr with a velocity spin up directly related to the plume break through shown in the top frame of Fig. 4. For the models with lower temperature contrast A and B the initial quiet period lasts longer and the episodes of velocity spin-up show a smaller Vrms amplitude. The correlation between the different quantities suggests that the episodes of increased convective vigor must be related to an increase in the temperature of the bottom 3PO layer with positive feedback from the temperature dependent electron conductivity. The interaction with the 3PO phase boundary with a strongly negative Clapeyron slope resisting whole mantle flow leads to the flushing events (e.g. Honda et al., 1993, Tackley et al., 1993, Steinbach et al, 1993) when large plumes break through the

ACCEPTED MANUSCRIPT

resisting phase boundary. At lower values of ΔT the effective bottom thermal conductivity is smaller and the time period necessary for heating up the bottom layer and reaching critical temperature takes longer.

We give the corresponding results to Fig. 16 for the constant conductivity model B in Fig. 17. These models are characterized by a penetrative convective regime with feeble convective vigor in the bottom half of the model and a low uniform conductivity, in agreement with low values of the surface heat flux, the rate of internal temperature and the rms velocity amplitudes.

Fig. 18 shows the overall breakdown of the composite conductivity for the different ΔT values used in the convection results. The corresponding temperature profiles are shown in Fig. 18a. The controlling effect of temperature and pressure on the different components of k is clearly illustrated. The electron thermal conductivity k_{el} becomes operational at $T > 5000K$ (see Fig. 3). Since the radiative component k_{rad} tapers off for $T > 5000K$, there is a thresholding effect and represents an effective switch from k_{rad} to k_{el} at this temperature. k_{el} is the dominant mechanism near the bottom boundary layer for the model with $\Delta T = 10,000K$.

The results presented sofar show clearly that an episodic type of deep mantle dynamics is produced by the interplay of thermal expansivity, thermal conductivity and the Clapeyron slope of the 3PO phase transition.

O'Neill and Lenardic (2007) have argued that super-Earth type terrestrial planets have a larger propensity for stagnant lid dynamics of the upper mantle as a result of the high pressure gradient in the shallow leading to surpressing brittle deformation mechanisms. This may have an impact also on episodic deep mantle dynamics. In the following we therefore investigate the impact of a stagnant lid on the model results. Stagnant lid convection occurs for sufficiently high viscosity contrasts around 10^5 to 10^6 (e.g. Moresi and Solomatov, 1995) To investigate the effects of stagnant lid convection in our models we have used an Arrhenius parameterization of the viscosity, defined in Table 2, in a model, labeled F in Table 5, with identical thermophysical parameters as in model C and a temperature contrast across the mantle $\Delta T = 10000$ K. Snapshots of depth profiles of relevant quantities for model F are given in Fig 19. The stagnant lid character of model F is illustrated in the profiles of the viscosity and the amplitude of the velocity field. The viscosity profiles show more than six orders of viscosity variation and a stagnant lid of about 300 km thickness. This is in agreement with the velocity profiles showing an effectively rigid outer surface and rapid increase of the flow velocity in the mantle below the lid. Temperature and conductivity profiles aer similar to the corresponding

profiles of model C shown in Fig. 13, except for a systematic increase of mantle temperature over time due to the decrease in in mantle cooling capacity in the presence of the stagnant lid.

Time series of global quantities for model F are shown in Fig. 20, corresponding to similar data for model C shown in Fig. 16. The episodic nature of the mantle dynamics for model F is most clearly illustrated by the Vrms curve in Fig. 20c which is much like the corresponding curve for the C model and $\Delta T = 10000$ K. Differences between results of the two models are; shorter time scale for model F, related to a combination of higher temperature and conductivity and lower viscosity in the deep mantle, compared to model C. Further, the mantle temeperature increases more, in the stagnant lid case F, as a consequence of the thermal resistance of the stagnant lid.

A snapshot of the temperature field from the results of the F model case is shown in Fig. 21 for a model time of 1.24 Gyr, close to the first of a double peak in Vrms, corresponding to a plume breaking through the 3PO phase boundary, visible in the snapshot. Compared to the corresponding mobile lid results in Fig. 4c (model C) and Fig. 9 (model E), cold downwellings are less significant in Fig. 21 as a result of the different stagnant lid conditions. This further illustrates the fact that the

Accepted Manuscript

ACCEPTED MANUSCRIPT

characteristic episodic deep mantle dynamics is mainly controled by the particular thermophysical parameters prevailing in the deep mantle of exo-solar planets. Therefore, plate dynamics on the surface do not exert any influence on deep mantle processes of exosolar planets.

4 Discussions and Concluding Remarks

Super-earth extrasolar planets are fundamentally different from the Earth in the pressure and temperature range of the different mantles and this particular aspect brings in more phase transitions and different heat transport mechanisms, unknown in the Earth's mantle and causes noticeable deviation from a thermal evolution predicted by parameterized convection (Sharpe and Peltier, 1978).

Our calculations address a number of important dynamical problems in thermal convection of super-Earth planets. However, we note that our model does have some shortcomings such as lack of density stratification, curvature from a spherical-shell model and also the assumption of a large core. However, all of these factors will conspire to induce greater degrees of layering in mantle convection.

An interesting outcome from our study is the development of a super-adiabatic layer of around 700 km, which coincides with the location of the 3PO phase transition. This relatively thick super-adiabatic layer will influence the amount of heat delivered from the core and the thermal evolution of the planet.

The major result from our work comes from the interplay between the strongly endothermic 3PO phase transition and the electronic thermal conductivity, which allows for the periodic build-up of thermal energy to be discharged across the bottom boundary layer in the form of coherent upwellings. This represents a new type of episodic dynamics in which focussed plumes are periodically generated, by the steep rise in the exponential temperature dependence of the thermal conductivity.

We have shown that the high value of the thermal conductivity in the bottom thermal boundary layer is the critical ingredient creating this new dynamics. This was done by reproducing similar episodic dynamics with a purely depth dependent conductivity model defined from a time averaged conductivity profile of a model case with a fully temperature and pressure dependent conductivity. This high degree of similarity shows that positive feedback from the temperature dependence of conductivity into the dynamics of plume formation is not a first order effect. This latter finding is somewhat similar to our earlier demonstration that significant delay in planetary secular cooling in models with temperature depedent phonon conductivity is mainly due to the average conductivity profile characterized by a sub-lithospheric conducitvity minimum in the shallow mantle creating a low conductivity zone (LCZ) (van den Berg et al., 2005).

Furthermore we have shown that the episodic plume dynamics occurs both in a mobile lid mantle convection regime obtained with an exponential parameterization of the viscosity, with modest tempareture dependence, and a stagnant lid regime, obtained with an Arrhenius type viscosity with more than six orders of viscosity variation due to temperature. The latter case is considered more representative for exosolar planets of the super-Earth type (O'Neill and Lenardic,2007). A stagnant lid regime of planetary convection with variable viscosity may be linked to plate tectonics through a plastic bifurcation (Trompert and Hansen, 1997) and may play a role also in exosolar planets (Valencia et al., 2007b). The robustness of the episodic mantle dynamics is an important result since it underlines the fact that parameterized convection models which do not capture episodicity are inadequate to model thermal evolution of large super-Earth type exosolar planets. Future work would need to incorporate both realistic equation of states (Umemoto et al, 2006, Valencia et al., 2009) and sphericity. But the major findings of electronic thermal conductivity should still be valid under these circumstances.

Accepted Manuscript

ACCEPTED MANUSCRIPT

Acknowledgements

We thank discussions with Phil Allen, Michel Jacobs, Radek Matyska, Joost van Summeren, Diane Valencia, Renata Wentcovitch and K. Umemoto. Constructive reviews of Craig O'Neil and an anonymous reviewer were very helpful for improving the manuscript. This research has been supported by the ITR grant from National Science Foundation given to the VLAB at the University of Minnesota. Computational resources were provided through the Netherlands Research Center for Integrated Solid Earth Science (ISES 3.2.5).

Accepted Manuscript

ACCEPTED MANUSCRIPT

References

[1] Badro, J., Rueff, J-P., Vanko, G., Monaco, G., Fiquet, G., and F. Guyot, Electronic transitions in perovskite: possible nonconvecting layers in the lower mantle, Science, 305, 383-386, 2004.

[2] Bean, J.L., Mc Arthur, B.E., Benedict, G.F. and A. Armstrong, Detection of a third planet in the HD 74156 system using Hobby-Eberly telescope, *Ap. J.*, **672**, 178-184, 2008.

[3] Breuer, D., Yuen, D.A. and T. Spohn, 1997, Phase transitions in the martian mantle: implications for partially layered convection *Earth Planet. Sci. Lett.*, **148**, 457-469.

[4] Bunge, H.P., Low plume excess temperature and high core heat flux inferred from non-adiabatic geotherms in internally heated mantle circulation models, *Earth Planet. Sci. Lett.*, **153**, 3-10, 2005.

[5] Christensen, U.R. and D.A. Yuen, Layered convection induced by phase transitions, *J. Geophys. Res.*, **90**, 10291-10300, 1985.

[6] Dubuffet, F., Yuen, D.A. and M. Rabinowcz, Effects of a realistic mantle thermal conductivity on the patterns of 3-D convection, *Earth and Planetary Science Letters*, **171**, 401-409, 1999.

[7] Dubuffet, F., Yuen, D.A. and E. Rainey, Controlling thermal chaos in the mantle by positive feedback from radiative thermal conductivity, *NONLINEAR PROCESSES IN GEOPHYSICS*, **9**, 3-4, 311-323, 2002.

[8] Haghighipour, N. and S.N. Raymond, Habitable planet formation in binary planetary systems, *Ap. J.*, **666**, 436-447, 2007.

[9] Hansen, U., Yuen, D.A., Kroening, S.E., and T.B. Larsen, Dynamical consequences of depth-dependent thermal expansivity and viscosity on mantle circulations and thermal structure, *Phys. Earth Planet. Inter.*, **77**, 205-223, 1993.

[10] Hofmeister, A.M., Mantle values of thermal conductivity and the geotherm from phonon lifetimes, *Science*, **283**, 1699-1706, 1999.

[11] Honda, S., Yuen, D.A., Balachandar, S. and D. Reuteler, Three-dimensional instabilities of mantle convection with multiple phase transitions, *Science*, **259**, 1308-1311, 1993.

[12] Jacobs, M.H.G. and B.H.W.S. de Jong, Placing constraints on phase equilibria and thermophysical properties in the system $MgO - SiO_2$ by a thermodynamically consistent vibrational method *Geochimica et Cosmochimica Acta*, **71**, 3660-3655, 2007.

[13] Jarvis, G.T. and D.P. McKenzie, Convection in a compressible fluid with infinite Prandtl number, *J. Fluid Mech.*, **96**, 525-583, 1980.

[15] Kokubo, E. and S. Ida, Formation of terrestrial planets from protoplanets, II *Statistics of planetary spin*, **671**, no. 2, 2082-2090, 2008.

[15] Marcy, G., Butler, R.P., Fischer, D., Vogt, S., Wright, J.T., Tinney, C.G. and H.R.A. Jones, Observed Properties of Exoplanets: Masses, Orbits, and Metallicities, *Progress of Theoretical Physics* Supplement No. 158, 1-19, 2005.

Accepted Manuscript

ACCEPTED MANUSCRIPT

[16] Matyska, C. and D.A. Yuen, Lower mantle properties and convection models of multiscale plunes, in: *Plates, Plumes, and Planetary Processes*, ed. G.R. Foulger and D.M. Jurdy, Geological Society of America Special Paper 430, 137-163, 2007.

[] Moresi L.-N. and V. S. Solomatov, Numerical investigation of 2D convection with extremely large viscosity variations, *Phys. Fluids*, **7**, 2154-2162, 1995.

[18] Katsura, T., Yokoshi, S., Kawabe, K., Shatskiy, A., Manthilake, M. A. G. M., Zhai, S., Fukui, H., Hegoda, H. A. C. I., Yoshino, T., Yamazaki, D., Matsuzaki, T., Yoneda, A., Ito, E., Sugita, M., Tomioka, N., Hagiya, K., Nozawa, A., Funakoshi, K.-I., P-V-T relations of MgSiO3 perovskite determined by in situ X-ray diffraction using a large-volume high-pressure apparatus, *Geophys. Res. Lett.*, **36**, L01305, doi:10.1029/2008GL035658, 2009.

[19] O'Neill, C. and A. Lenardic, Geological consequences of super-sized Earths, *Geophys. Res. Lett.*,**34**, L19204, doi:10.1029/2007GL030598, 2007.

[20] Perryman, M.A.C., Extra-solar planets, *Rep. Prog. Phys.*, **63**, 1209-1272, 2000.

[21] Queloz, D. (et al.), The CoRoT-7 planetary system: two orbiting Super-Earths, *Astronomy and Astrophysics*, manuscript no. corot7revisedv0, August 24, 2009.

[22] Sharpe, H.N., and W.R. Peltier, Parameterized mantle convection and the Earth's thermal history, *Geophys. Res. Lett.*, **5**, 737-740, 1978.

[23] Steinbach, V., Yuen, D.A. and W. Zhao, Instabilities from phase transitions and the timescales of mantle evolution, *Geophys. Res. Lett.*, **20**, 1119 -1122, 1993.

[24] Tackley, P.J., On the penetration of an endothermic phase-transition by upwellings and downwellings *J. Geophys. Res.*, **100**, B8, 15,477-15,488, 1995.

[25] Tackley, P.J., Stevenson, D.J., Glatzmaier, G.A. and G. Schubert, Effects of an endothermic phase transition at 670 km depth in a spherical model of convection in the Earth's mantle, *Nature*, **361**, 699-704, 1993.

[26] Trompert, R. and U. Hansen, Mantle convection simulations with rheologies that generate plate-like behavior, *Nature*, **395**, 686-689, 1998.

[27] Tsuchiya, T., Tsuchiya, J., Umemoto, K. and R.M. Wentzcovitch, Phase transition in MgSiO3 perovskite in the earths lower mantle, Earth Planet. Sci. Lett., 224, 241-248, 2004.

[28] Umemoto, K., Wentzcovitch, R.M., Allen, P.B., Dissociation of MgSiO3 in the cores of gas giants and terrestrial exoplanets, Science, 311, 983-986, 2006.

[29] Valencia, D., Connell, R.J., Sasselov, D., Internal structure of massive terrestrial planets, *Icarus*, 181, 545-554, 2006.

[30] Valencia, D., Sasselov, D. and R.J. Connell, Radius and structure models of the first super-earth planet, *The Astrophysical Journal*, **656**, 545-551, 2007a.

[31] Valencia, D., OConnell, R.J. and D.D. Sasselov, Inevitability of plate tectonics on super-earths, *The Astrophysical Journal*, **670**, 45-48, 2007b

Accepted Manuscript

ACCEPTED MANUSCRIPT

642 [32] van den Berg, A.P., van Keken, P.E. and D.A. Yuen, The effects of a composite non-Newtonian
643 and Newtonian rheology in mantle convection, Geophys. J. Int., 115, 62-78, 1993.

644 [33] van den Berg, A.P. and D.A. Yuen, Modelling planetary dynamics by using the temperature at
645 the core-mantle boundary as a control variable: effects of rheological layering on mantle heat
646 transport, *Phys. Earth Planet. Inter.*, **108**, 219-234, 1998.

647 [34] van den Berg, A.P., Yuen, D.A. and V. Steinbach, The effects of variable thermal conductivity
648 on mantle heat-transfer, *Geophys. Res. Lett.*, **28**, 875-878, 2001.

649 [35] van den Berg, A.P., Rainey, E.S.G. and D.A. Yuen, The combined influences of variable ther-
650 mal conductivity, temperature- and pressure-dependent viscosity and core-mantle coupling on
651 thermal evolution Phys. Earth Planet. Inter., 149, 259-278, 2005.

652 [36] van Summeren, J.R.G., van den Berg, A.P. and R.D. van der Hilst, Upwellings from a deep
653 mantle reservoir filtered at the 660 km phase transition in thermo-chemical convection models
654 and implications for intra-plate volcanism, *Phys. Earth Planet. Inter.*, **172**, 210-224, 2009.

Accepted Manuscript

ACCEPTED MANUSCRIPT

A Density parameterization

We consider a simple two layer model of a planet consisting of a homogeneous core and mantle with contrasting uniform densities ρ_c and ρ_m respectively. Assuming a uniform density mantle is consistent with the use of an extended Boussinesq formulation of the mantle convection equations applied in our modelling experiments. The two layer model is set up for a planet of given mass M. We further assume the mass fraction of an assumed metal core X_c to be given. In the modelling experiments we set $X_c = 0.315$, equal to the Earth value.

The model can then be formulated in terms of the volume average densities of the core ρ_c and mantle ρ_m. This way the outer planet radius R and the core radius R_c can be expressed in terms of M, X_c and $\rho_c,\ \rho_m$.

As a first approximation of cases with a self-compressing planet we consider several models which are related by a simple uniform compression factor, taken to be identical for the mantle and core. In the 2-D ρ_c, ρ_m parameter space these models are located on a line with fixed ρ_c/ρ_m. This parameterization can be used to study in a simple way the effect of compression on the internal gravity and pressure distribution.

In the following expressions are derived for the outer radius of the planet and its core in terms M, X_c, ρ_c, ρ_m. For the total planetary mass we have,

$$M = M_c + M_m = X_c M + (1 - X_c)M \tag{11}$$

The core radius is derived from the core mass fraction as,

$$R_c = R\left(1 + \frac{\rho_c}{\rho_m}\left(\frac{1}{X_c} - 1\right)\right)^{-1/3} \tag{12}$$

An expression for the outer radius is derived from the total mass as,

$$R^3 = \frac{3M}{4\pi}\left(X_c\frac{1}{\rho_c} + (1 - X_c)\frac{1}{\rho_m}\right) \tag{13}$$

With the non-dimensionalization scheme, $M = M'M_0$, $R = R'R_0$, $\rho_c = \rho'_c\rho_0$, $M_0 = \rho_0 V_0 = \rho_0\frac{4\pi}{3}R_0^3$, we get,

$$R'^3 = M'\left(X_c\frac{1}{\rho'_c} + (1 - X_c)\frac{1}{\rho'_m}\right) \tag{14}$$

For the special case of a uniform sphere with $M' = 1$ this expression produces a unit non-dimensional outer radius $R' = 1$ with $\rho_c = \rho_m = \rho_0$ and $\rho'_c = \rho'_m = 1$.

For the core radius we get with the same non-dimensionalization scheme,

$$R'_c = R'\left(1 + \frac{\rho'_c}{\rho'_m}\left(\frac{1}{X_c} - 1\right)\right)^{1/3} \tag{15}$$

Explicit expressions for the core and mantle densities can be derived from the above for R' and R'_c.

$$\rho'_c = \frac{X_c M'}{R'^3_c} \tag{16}$$

$$\rho'_m = \frac{M'(1 - X_c)}{R'^3 - R'^3_c} \tag{17}$$

Accepted Manuscript

ACCEPTED MANUSCRIPT

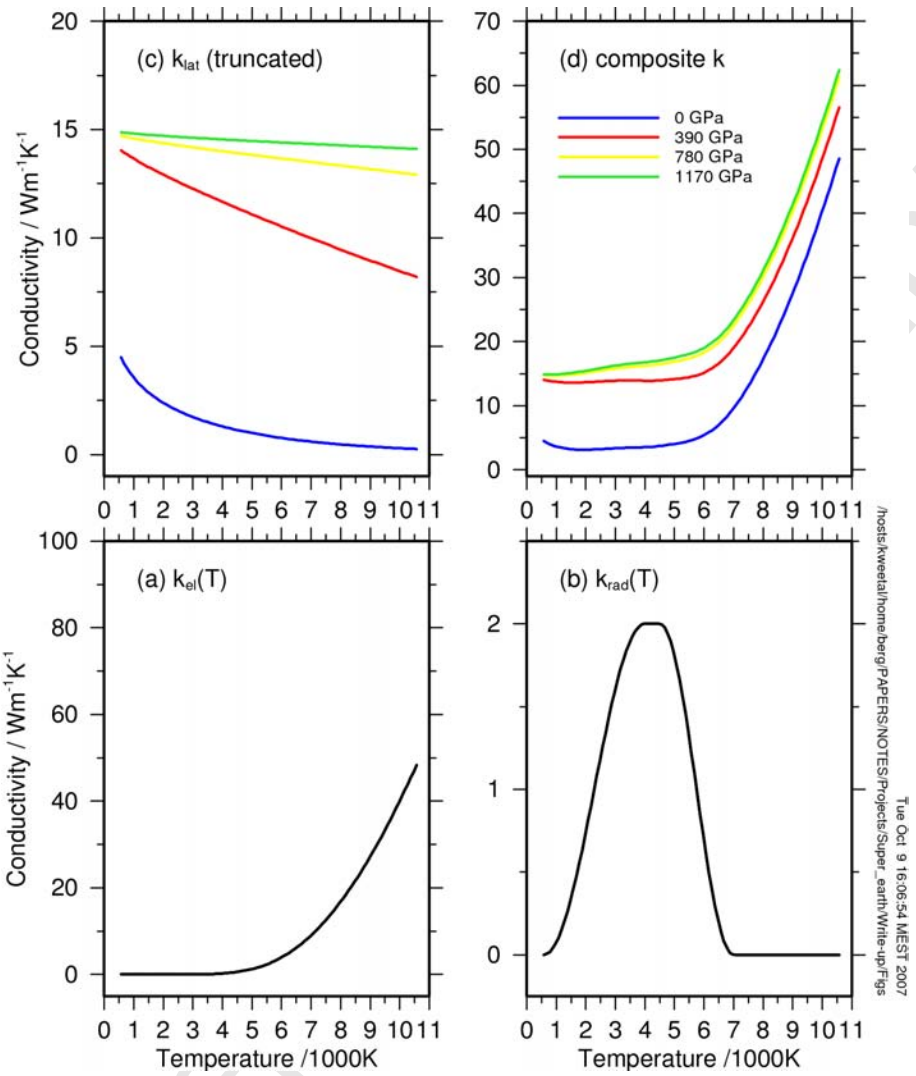

688

Figure 3: *Components of the composite condivity model. Frames (a) and (b) show the distributions of the electron conductivity and radiative conductivity respectively which are independent of pressure. Frame (c) shows the lattice conductivity, at different values of pressure, using a truncation value at high pressure of* $15 W m^{-1} K^{-1}$. *Frame (d) shows the corresponding effective conductivity. Color coding of the pressure values* $P_i, 0, 390, 780, 1170 GPa$ *is indicated in the plot legend.*

ACCEPTED MANUSCRIPT

689

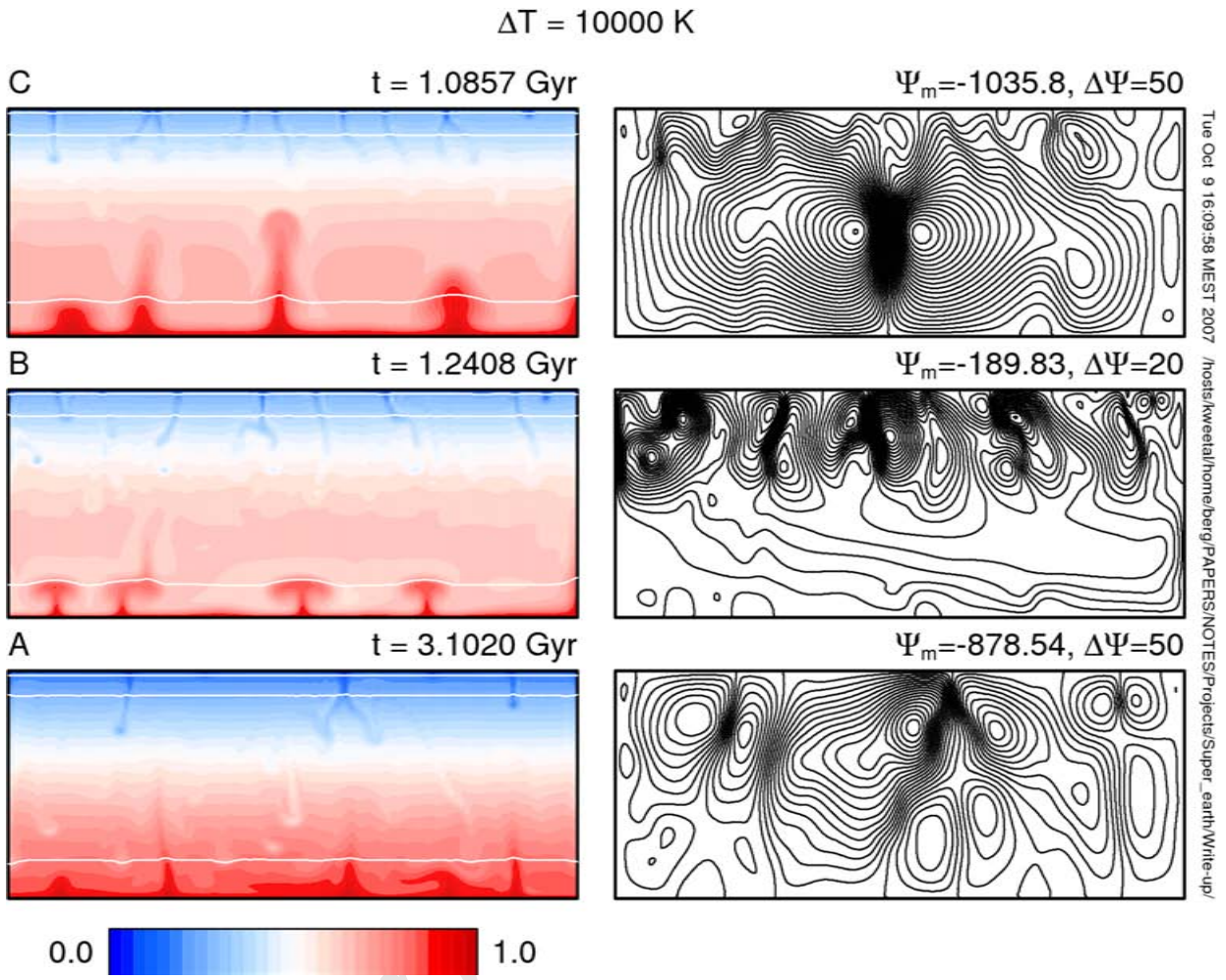

Figure 4: *Snapshots of non-dimensional temperature (left) and streamfunction (right) for different models A,B,C defined in Table 5, for the same temperature contrast across the layer* $\Delta T = 10,000K$. *White lines indicate the instantaneous position of the three phase boundaries included in the model.*

Accepted

ACCEPTED MANUSCRIPT

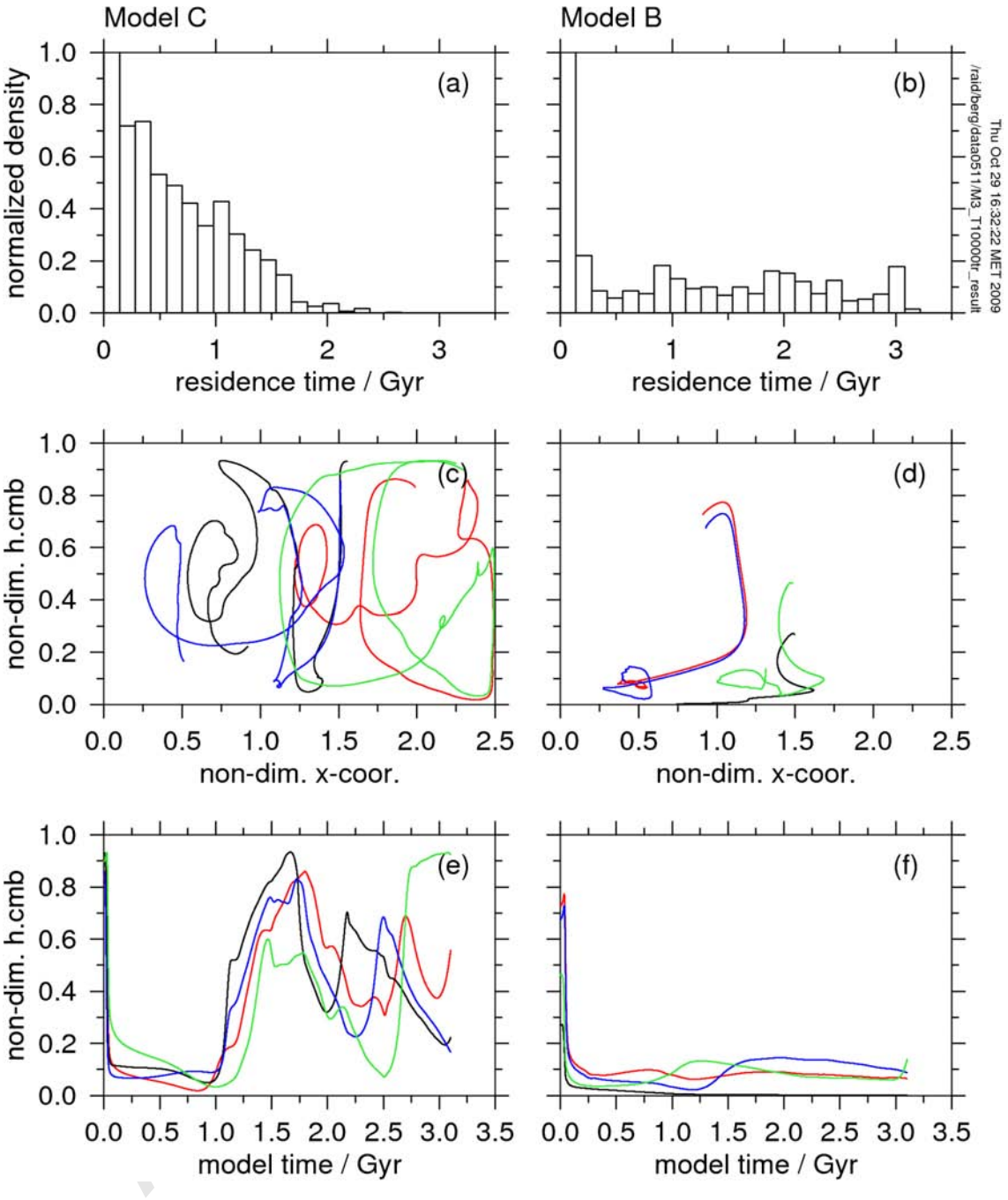

690

Figure 5: *Comparison of different convective layering characteristics between models C (lefthand column of frames) and B (righthand) defined in Table 5. (a) and (b) show histograms of residence time values in the bottom 3PO phase layer for 2000 randomly distributed particle tracers that are advected by the convective flow. Histograms have been normalized normalized identically to obtain a unit integral value over residence time. The maximum values of the first bins 2.45 (model C) and 4.87 (model B) has been clipped at unit value. Frames (c) and (d) show trajectories for four tracers taken from representative residence time bins, $\tau = 1$ Gyr (Model C) and $\tau = 3$ Gyr (Model B) respectively. Frames (e) and (f) show the non-dimensional height above the CMB versus model*

ACCEPTED MANUSCRIPT

time for the same tracers of (c) and (d).

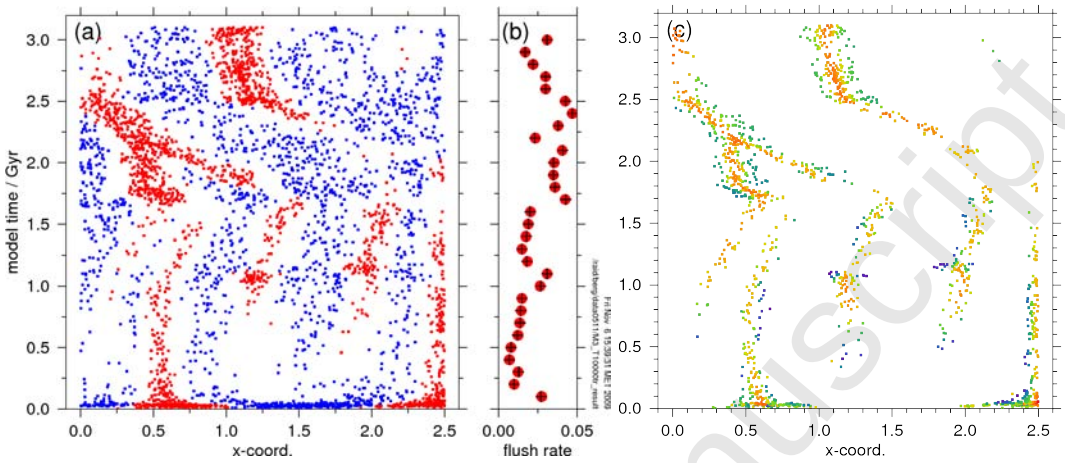

Figure 6: *(a) phase boundary crossing events at the 3PO transition displayed by the horizontal and time coordinates of passive tracers monitoring the local mineral phase for model C. Red (1864) and blue (1877) symbols represent upward and downward crossings respectively. (b) upward mass flux through the 3PO boundary estimated by (100 Myr) time binned values of the number of upward phase boundary crossings normalized by the total number of tracers in the domain. Red dots indicate results based on the full data set of 2000 tracer particles. The black crosses showing test results computed from half the data set indicate that a sufficient number tracers were used. (c) Color coded temperature values of upward monitor crossings of the depthlevel 0.9 times the layer depth, inside the 3PO layer, for model C. The number of upward crossing events is 1387. A rainbow palette has been used indicating temperature variation between 7000 K and 10,000 K. The hotter cores of plumes can be distinguished from the cooler off-central parts of the upwellings. Episodic broadening of the upwelling flows is in agreement with the episodic dynamics of the 3PO layer which is reinforced by a positive feedback related to the temperature dependence of the conducitvity.*

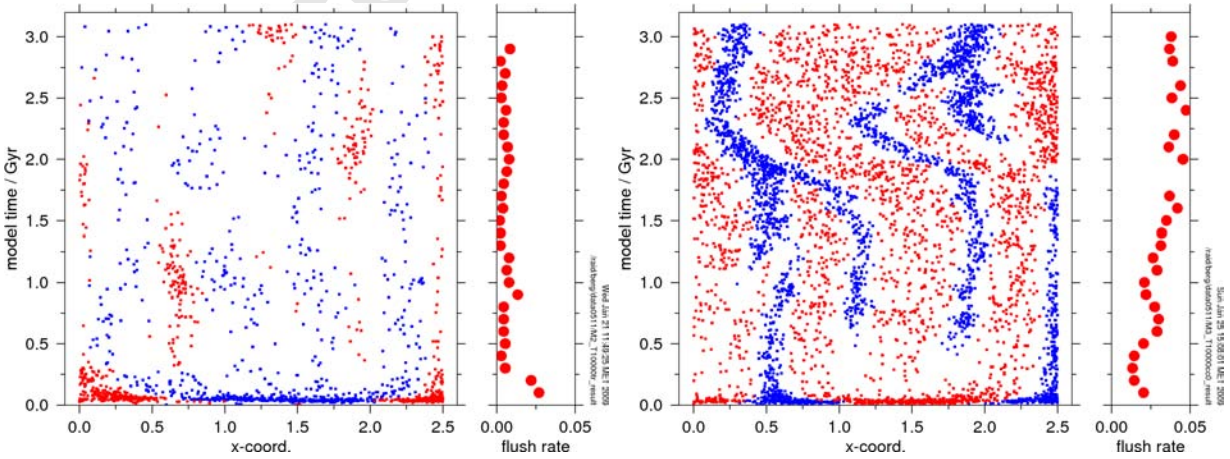

Figure 7: *Similar results as in Fig.6 the uniform conductivity model B (left). The number of up- and downward phase boundary crossing events is 772 and 774 respectively. The two rightand frames*

ACCEPTED MANUSCRIPT

show similar data for a modelrun with the same parameters as the variable conductivity model C except that the Clapeyron slope of the 3PO phase transition has been set to zero (right hand results). The number of up- and downward phaseboundary crossing events is 2506 and 2514 respectively.

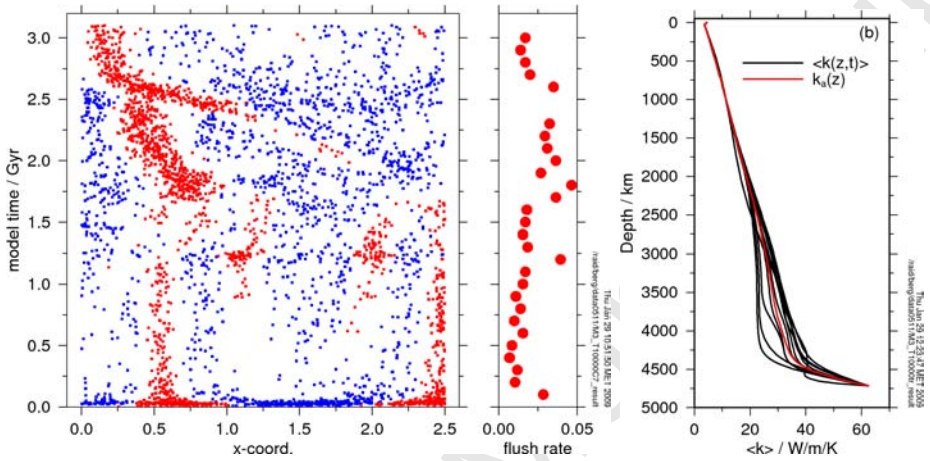

693

Figure 8: *(a) (3PO)phase boundary crossing events for model E with purely depth dependent conductivity showing similar results as in Fig.6a. The number of upward and downward events is 1819 and 1821 respectively. (b) Conductivity depth profile used for model E shown in red, computed by timeaveraging $k(z,t)$ profiles from model C shown in black.*

694

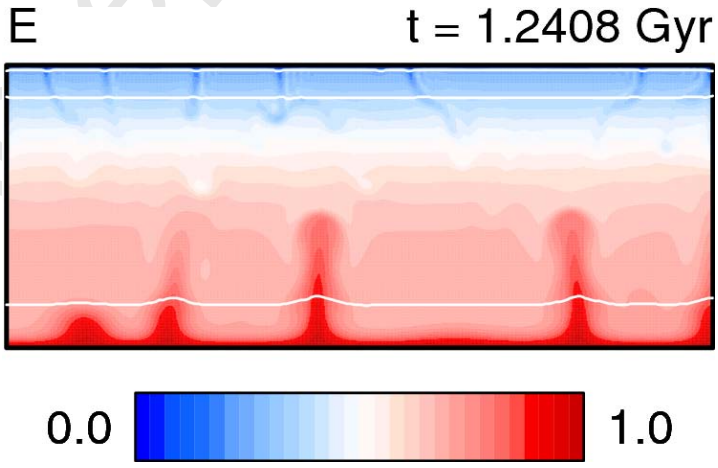

Figure 9: *Temperature snapshot of the depth dependent conductivity model E, showing very similar dynamics of large plume breakthrough as in Fig 4 for the P,T dependent variable conductivity model C.*

ACCEPTED MANUSCRIPT

695

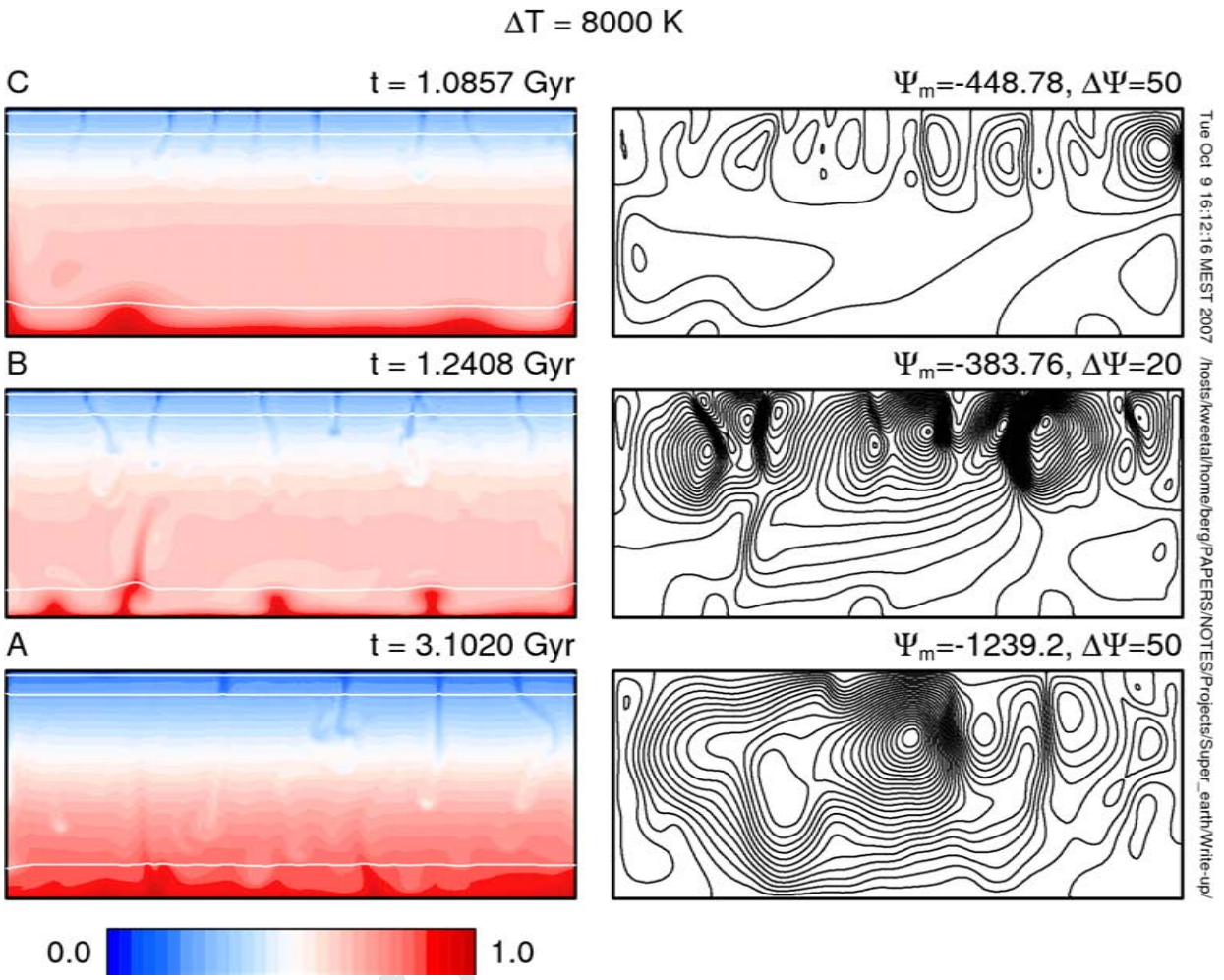

Figure 10: *Temperature and streamfunction snapshots for models similar to Fig. 4 but with a temperature contrast $\Delta T = 8000K$ across the mantle. The contrast between the B and C models has become significantly smaller due to the much smaller value of the conductivity near the bottom. This is a result of the reduced temperature and the strong temperature dependence of the electronic conductivity component which is dominent in the results shown in Fig. 4.*

Accepted

ACCEPTED MANUSCRIPT

696

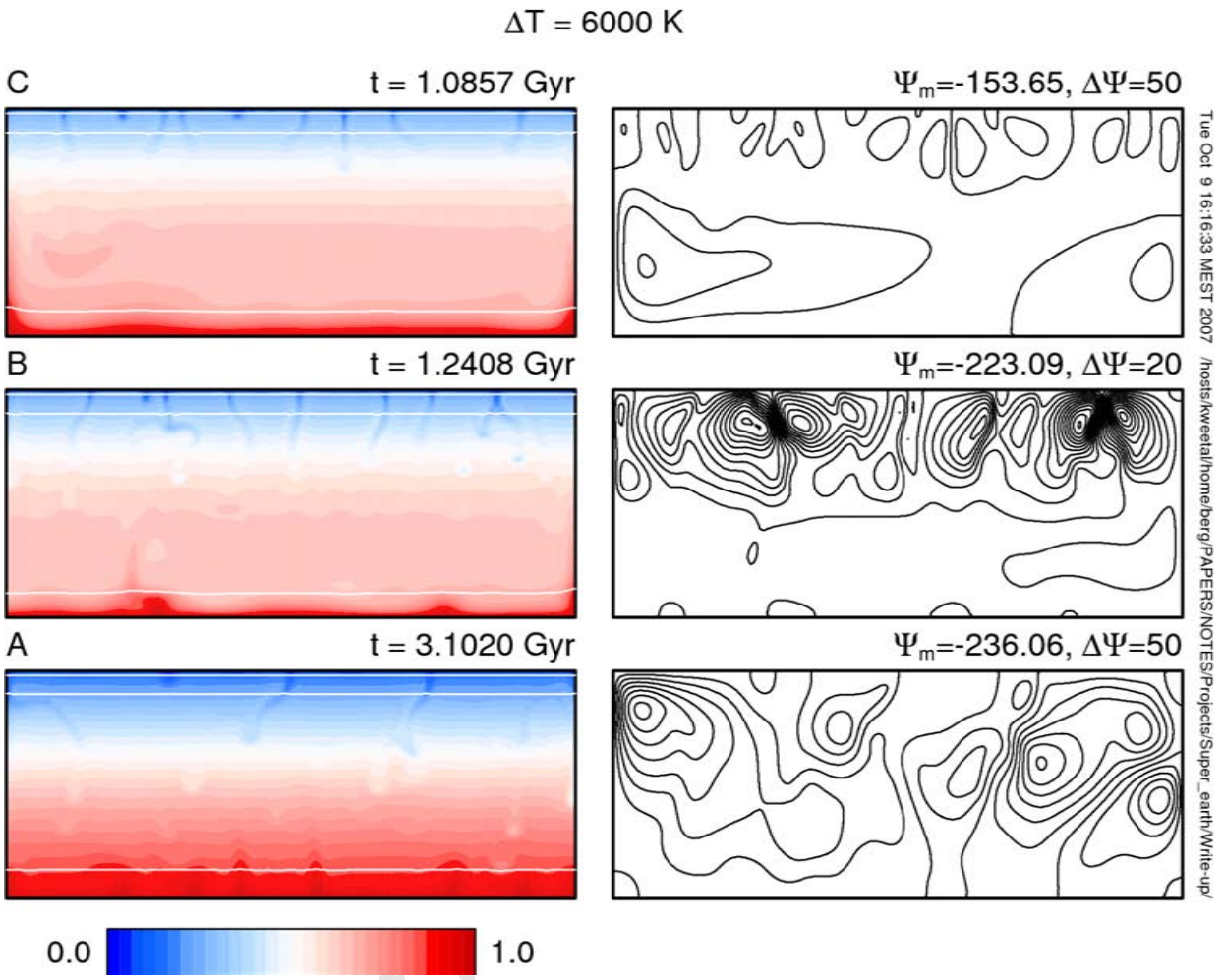

Figure 11: *Temperature and streamfunction snapshots for models similar to Fig. 4 but with a reduced temperature contrast $\Delta T = 6000K$ across the mantle. The contrast between the B and C models has become significantly smaller due to the much smaller value of the conductivity near the bottom. This is a result of the reduced temperature and the strong temperature dependence of the electronic conductivity component which is dominant in the results shown in Fig. 4.*

Accepted

ACCEPTED MANUSCRIPT

697

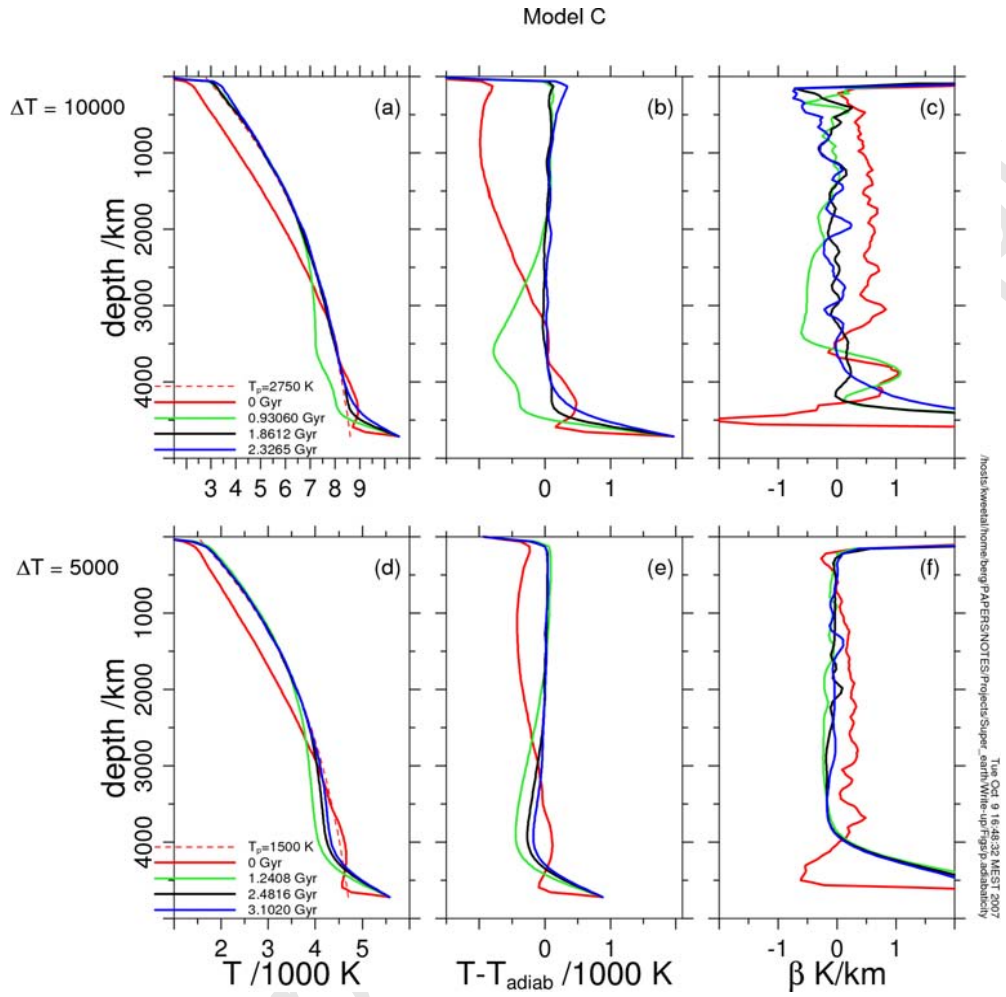

Figure 12: *Vertical profiles illustrating the time dependent degree of adiabaticity of the mantle for two endmember model cases, of type C defined in Table 5, with different temperature contrast across the mantle,* $\Delta T = 10,000K$ *top row (a),(b),(c) and* $\Delta T = 5000K$ *bottom row (d),(e),(f). The lefthand column (a),(d) shows snapshots of the horizontally averaged temperature at different time instances indicated in the legend. The red dashed line indicates an adiabatic temperature profile with potential (surface) temperature of* $2750K$ *(a) and* $1500K$ *(d) visually selected to overlap with the evolving geotherms. The middle column (b) and (e) shows snapshots of the difference between the mantle temperature profile and the reference adiabat. The righthand column shows corresponding profiles of the deviation of the local temperature temperature gradient from the adiabatic value defined in (10).*

ACCEPTED MANUSCRIPT

698

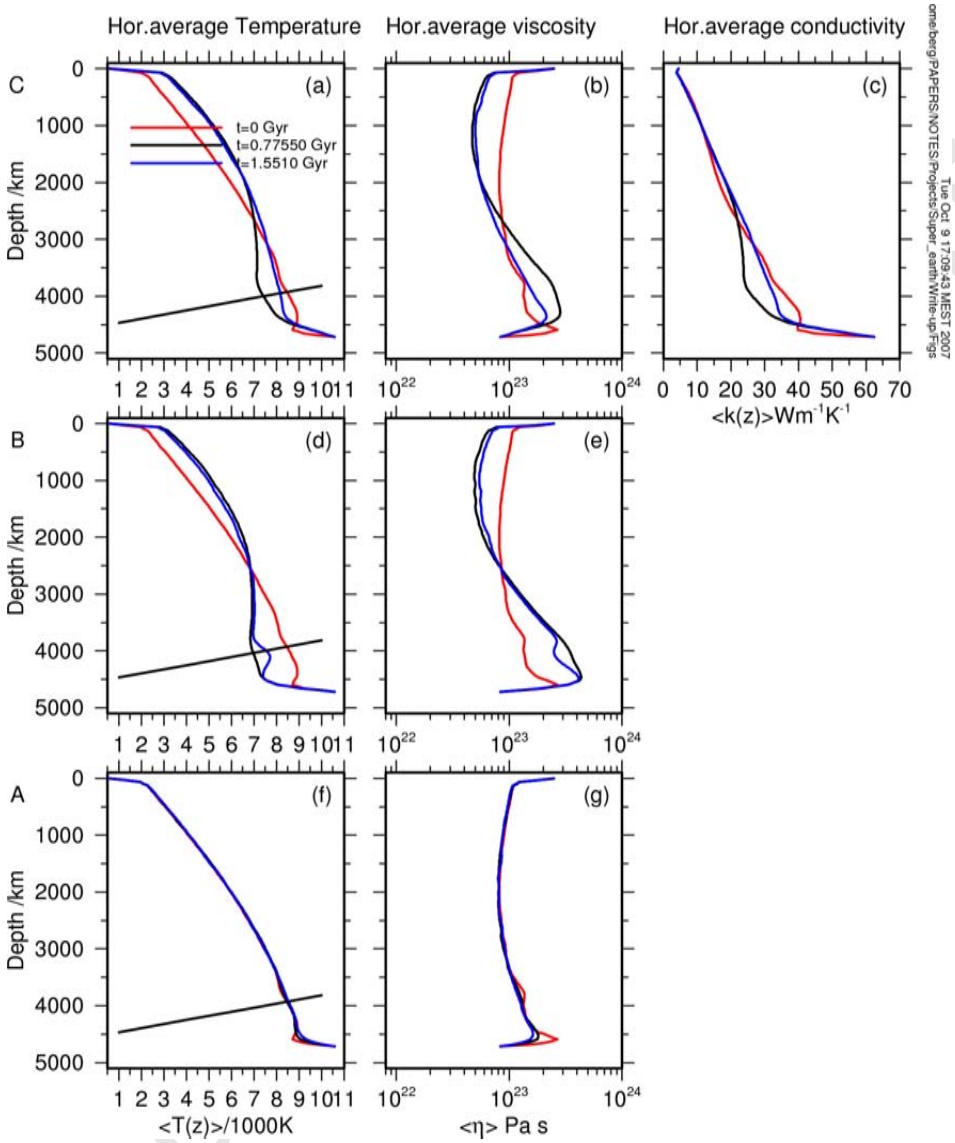

Figure 13: *Horizontal average depth profiles of temperature (left column) viscosity (middle) and thermal conductivity (right), for three models A (bottom row), B (middle row) and C (top row) shown in Fig.4. The temperature contrast across the mantle is fixed at* $\Delta T = 10,000K$ *for all cases. The Clapeyron curve of the 3PO phase is indicated by the straight black line in frames (a),(d),(f).*

ACCEPTED MANUSCRIPT

699

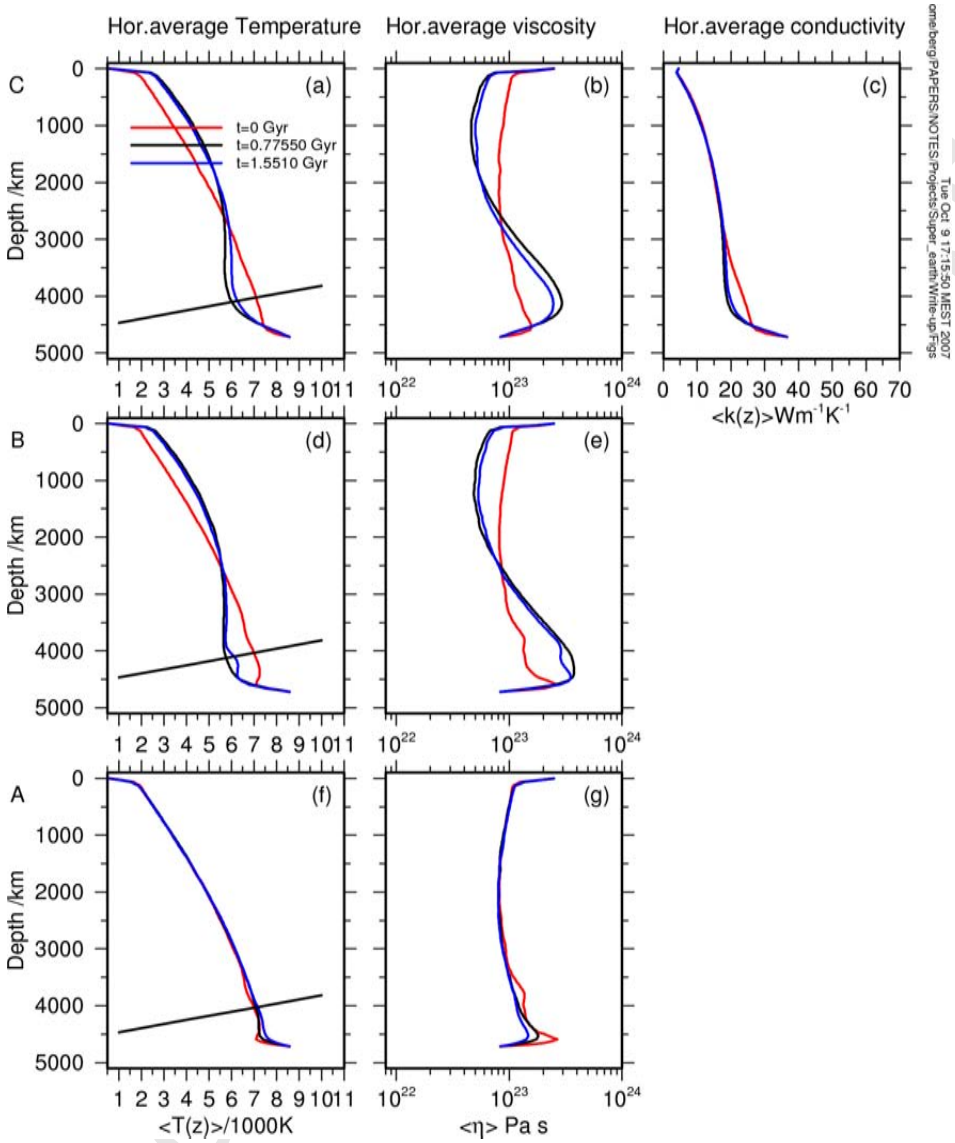

Figure 14: *Similar profiles as in Fig. 13 but now for a temperature contrast across the mantle* $\Delta T = 8000K$.

ACCEPTED MANUSCRIPT

700

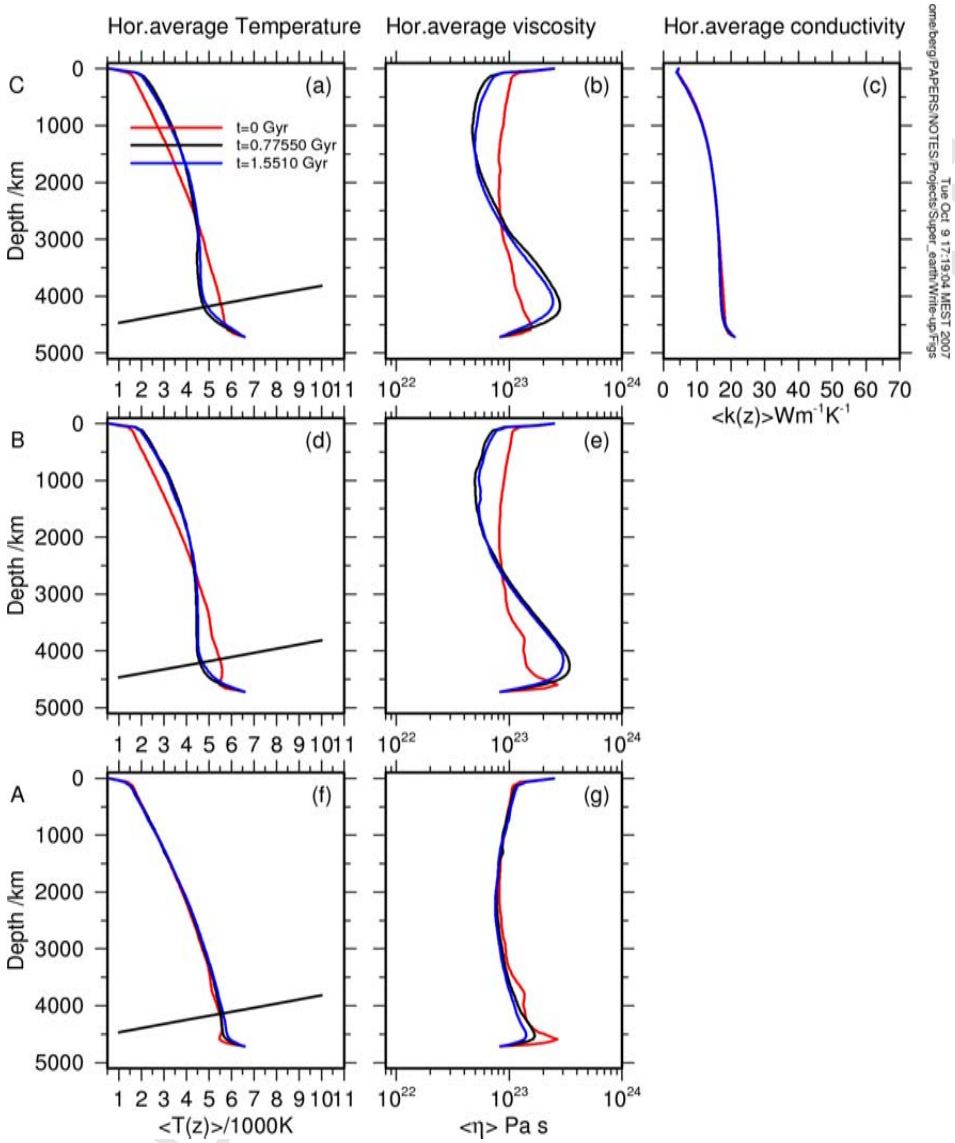

Figure 15: *Similar profiles as in Fig. 13 but now for a temperature contrast across the mantle* $\Delta T = 6000K$.

ACCEPTED MANUSCRIPT

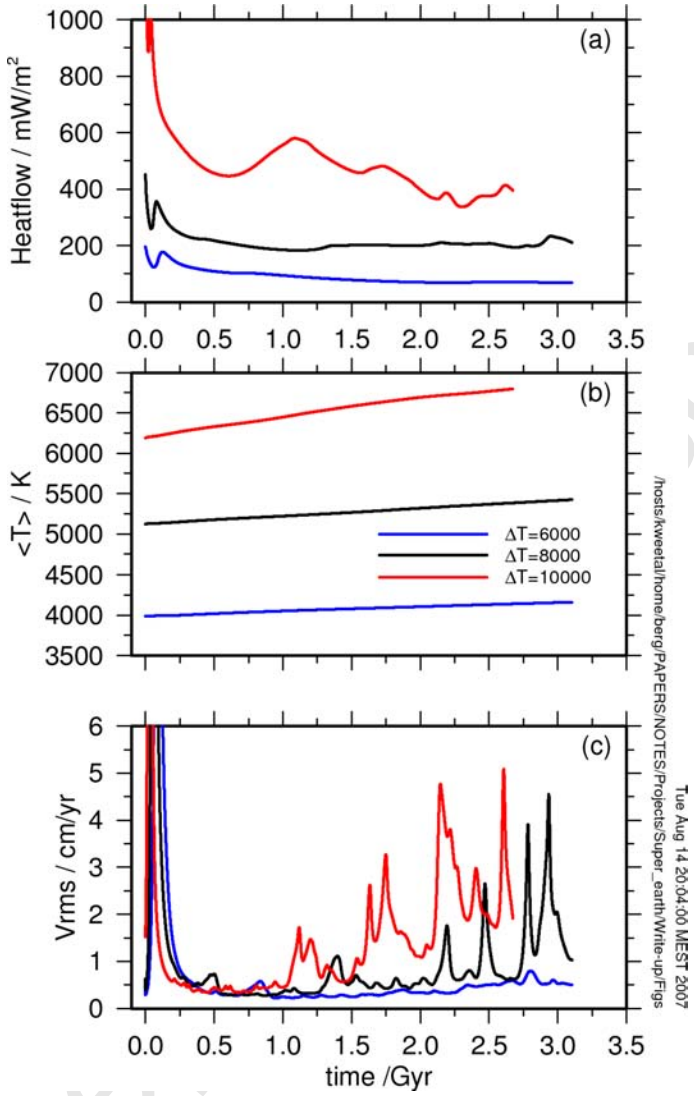

701

Figure 16: *Timeseries of (a) bottom heat flux, (b) volume average temperature and (c) root-mean-squared velocity for the variable conductivity models C. Three values of the mantle temperature contrast ΔT are considered, 6000 (blue), 8000 (black) and 10,000 K (red).*

ACCEPTED MANUSCRIPT

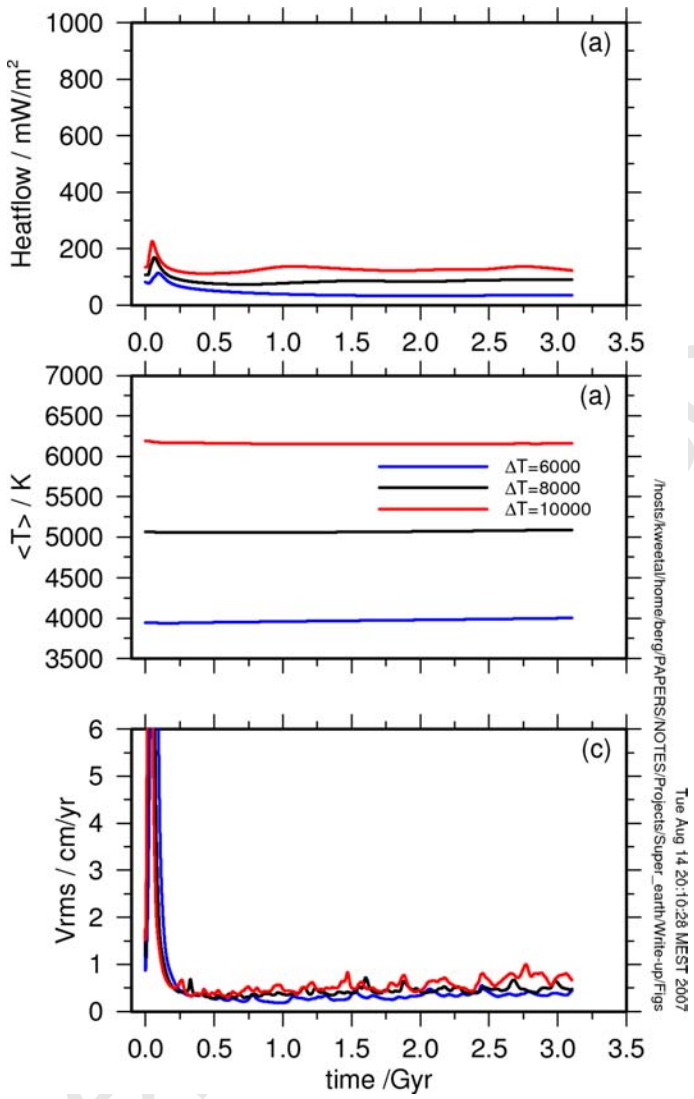

Figure 17: *Similar timeseries as in Fig. 16 for the constant conductivity models B with thermal expansivity contrast* $\Delta\alpha = 0.05$. *These uniform k models show no global warming and much lower bottom heat flux than shown in Fig. 16. The low Vrms values are in agreement with penetrative convection without large scale mass transport through the 3PO interface.*

ACCEPTED MANUSCRIPT

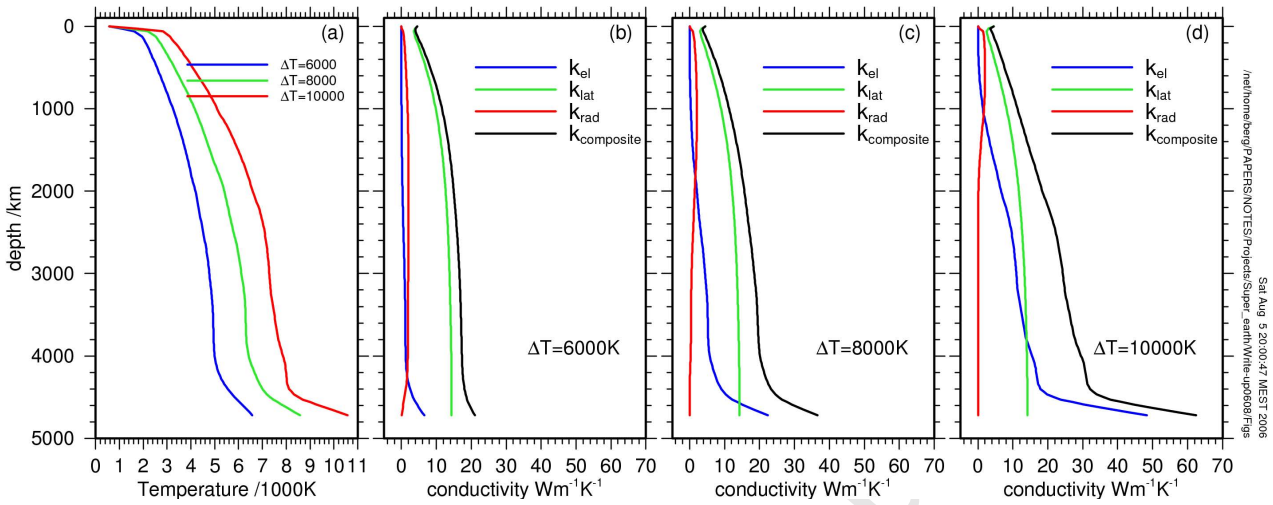

Figure 18: *Temperature depth profiles and corresponding decomposition of the variable conductivity for three values of the temperature contrast ΔT across the mantle. (a) temperature. (b,c,d) corresponding conductivity (k-component) profiles.*

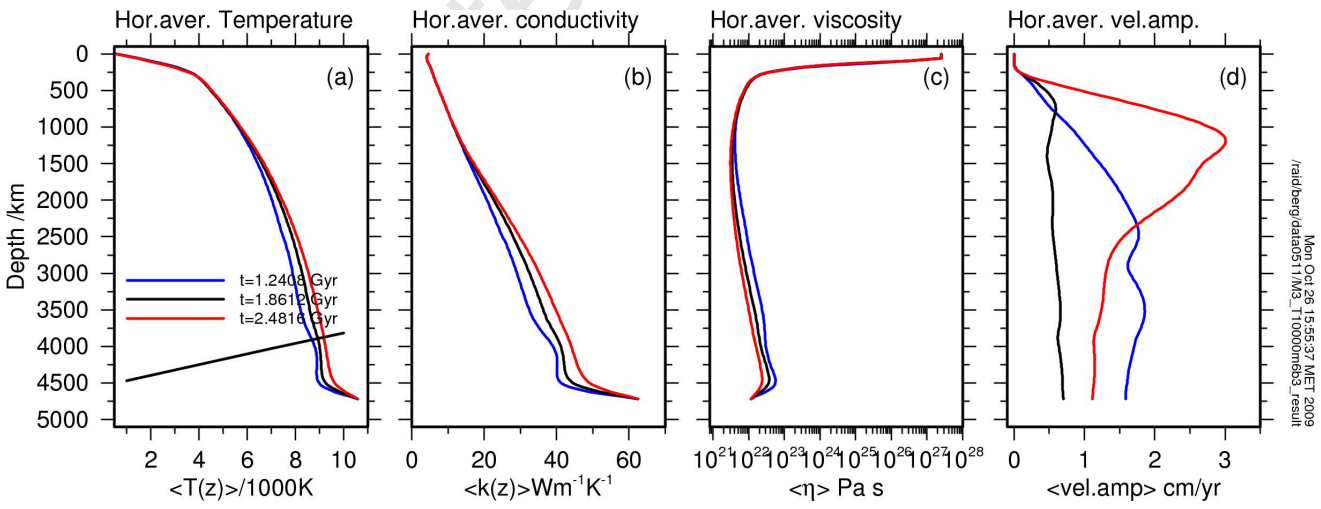

Figure 19: *Depth profiles of horizontally averaged temperature (a), conductivity (b), viscosity (c), and magnitude of velocity (d) for three snapshots labeled by the model time value in frame (a). The Clapeyron curve of the 3PO transition is drawn in the lefthand frame to indicate the approximate location of the phase boundary. The viscosity varies by six orders of magnitude due to temperature in the shallower part of the model. This results in stagnant lid convection as illustrated by the vertical distribution of the velocity amplitude indicating an approximately 300 km thick immobile lid.*

ACCEPTED MANUSCRIPT

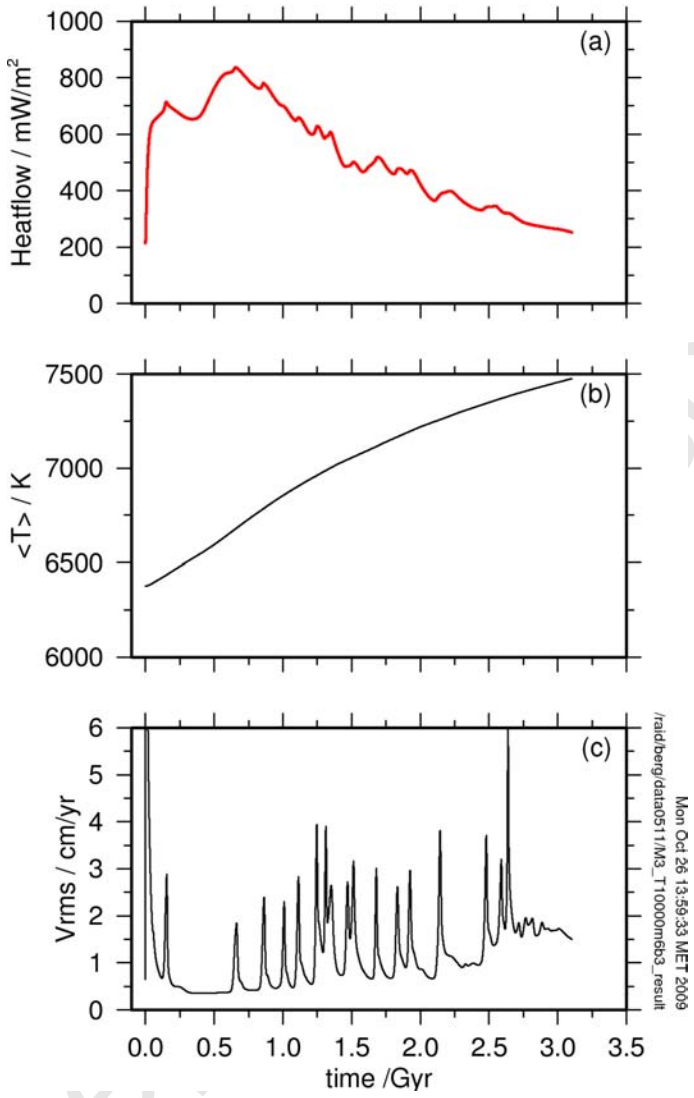

Figure 20: *Time series of global quantities for the stagnant lid model F: (a) CMB heatflow, (b) volume average temperature and (c) rms velocity amplitude. The dynamics of model F is similar as in model C, as characterized by the episodic behavior of hot plumes breaking through the 3PO phase boundary, producing sharp peaks in Vrms. Model F shows sharper peaks than model C which is related to the greater viscosity contrast due to temperature and lower viscosity in the bottom region near the 3PO transition.*

ACCEPTED MANUSCRIPT

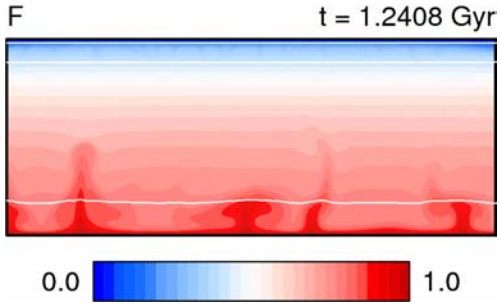

Figure 21: *Temperature snapshot for the stagnant lid model F. Different stages of interaction between hot plumes and the 3PO phase boundary are illustrated, varying from deflection (right), breaktrough (second from left) and regular flow through (second from right).*

Accepted Manuscript